Strong-Form Collocation Method for Solidification and Mechanical Analysis of Polycrystalline Materials

Ashkan Almasi[1]; Andrew Beel[2]; Tae-Yeon Kim[3]; John G. Michopoulos[4]; and Jeong-Hoon Song, M.ASCE[5]

Abstract: Materials engineering problems related to polycrystalline solids often require the prediction of grain growth and the stress analysis of polycrystalline materials. This study presents the particle difference method (PDM) as a reliable computational method applicable to this class of engineering problems. The PDM is a meshfree collocation method that directly discretizes the strong form of the governing partial differential equations based on Taylor series approximation and the moving least-squares approach. The PDM was applied to polycrystalline solids in the context of two-dimensional grain growth solidification and stress analysis of the resulting polycrystalline morphology. First, the PDM was used to predict grain growth during the solidification process of polycrystalline materials using a multiphase field model. Then the resulting morphology of the polycrystalline solids was adopted for successive stress analysis of the polycrystalline solids. Results from these analyses were compared with the results from the conventional finite-element method to verify the accuracy and efficacy of the PDM.
DOI: 10.1061/(ASCE)EM.1943-7889.0001665.

Introduction

The conventional finite-element methods (FEMs) have difficulties handling moving boundary or interface problems such as phase changes or problems with complex internal boundaries. The methods often employ remeshing or *h*-adaptive techniques to ensure the requisite accuracy near the interface. However, such approaches often entail cumbersome computations as well as the projection of field variables between existing and newly generated meshes, leading to a degradation of accuracy.

To circumvent these difficulties, various types of meshfree methods, including weak form–based meshfree and strong form–based collocation methods have been developed. Examples of these methods include the smoothed particle hydrodynamics (Gingold and Monaghan 1977), the diffuse-element method (Nayroles et al. 1992), the element-free Galerkin method (Belytschko et al. 1994), the reproducing kernel particle methods (Liu et al. 1995), *h*-*p* clouds (Duarte and Oden 1996), the finite-point method (Onate et al. 1996), the meshless local boundary integration method (Zhu et al. 1998), the meshless local Petrov–Galerkin method (Atluri et al. 1999), and the meshless point collocation methods (Aluru 2000). Although these methods do not require a mesh for the discretization of the governing partial differential equations, they often suffer from required additional computational cost for the computations of the shape functions and their derivatives. For example, strong form–based collocation methods require the computation of higher-order derivatives compared with Galerkin methods due to the direct discretization of the strong form. Thus, the strong form–based collocation methods require additional high computational cost to obtain shape functions and all their higher-order derivatives up to the order of the governing equations of the problem; the computational cost of these meshfree methods is often at least an order of magnitude higher than that of the conventional mesh-based method.

To address this issue, the particle difference method (PDM) was developed based on the key concept of approximating higher-order derivatives without separately computing them as in the conventional meshfree method. The key idea of the proposed method is based on computing discretized higher-order derivative operators with a Taylor expansion through the moving least-squares approach. Such ideas also were initially explored for meshfree methods by other researchers (Li and Liu 1999a, b; Kim and Kim 2003; Hillman and Chen 2016) with a different name. However, the approach was further developed by Yoon and Song (2014a, b, c) with the names of the PDM for continuum (Yoon and Song 2014b, c) and the extended particle difference method (EPDM) for moving interface problems (Yoon and Song 2014a). Another interesting alternative approach, a superconvergent meshfree collocation method (Wang et al. 2018), was proposed to reduce the cost of higher-order derivative computations and resolve the basis degree discrepancy in meshfree collocation formulations. In contrast to other existing meshfree and collocation methods, the PDM is capable of computing higher-order derivatives of the shape functions in the process of calculating the shape functions without further cost. Moreover, the method does not require the regularity of the weight function to ensure the regularity of the shape functions. Although the PDM shares the principal attractive features of other meshfree methods for modeling complex problems, the PDM is also particularly easy to implement compared with other meshfree methods. In particular, adaptive discretization refinement can be effectively treated in a simple manner. As a consequence, the PDM can simplify modeling of the evolution of moving boundary (or interface) and discontinuity problems such as crack propagations and phase changes. It also does not require numerical integration due to the

[1]Graduate Research Assistant, Dept. of Civil, Environmental, and Architectural Engineering, Univ. of Colorado, Boulder, CO 80309.

[2]Graduate Research Assistant, Dept. of Civil, Environmental, and Architectural Engineering, Univ. of Colorado, Boulder, CO 80309.

[3]Assistant Professor, Dept. of Civil Infrastructure and Environmental Engineering, Khalifa Univ. of Science and Technology, Abu Dhabi 127788, United Arab Emirates.

[4]Senior Research Scientist and Mechanical Engineer, Computational Multiphysics Systems Laboratory, Naval Research Laboratory, Washington, DC 20375.

[5]Assistant Professor, Dept. of Civil, Environmental, and Architectural Engineering, Univ. of Colorado Boulder, Boulder, CO 80309 (corresponding author). ORCID: https://orcid.org/0000-0002-2932-440X. Email: jh.song@colorado.edu

Note. This manuscript was submitted on October 5, 2018; approved on March 18, 2019; published online on August 9, 2019. Discussion period open until January 9, 2020; separate discussions must be submitted for individual papers. This paper is part of the ***Journal of Engineering Mechanics***, © ASCE, ISSN 0733-9399.

direct discretization of the governing equations. The PDM has been successfully applied to various problems such as Poisson and Stokes problems (Kim and Kim 2003), elastic crack growth and interface problems (Yoon et al. 2007; Liu et al. 2007; Yoon et al. 2006), dynamic crack propagation (Lee et al. 2016), and polycrystalline growth problems (Song et al. 2018; Fu et al. 2017).

The main objective of this paper was to further demonstrate the capabilities of the PDM in solving mechanics problems. The novelty and intellectual contribution of the paper originates from applying recently developed strong form–based collocation method to polycrystalline materials to assess the feasibility of the method in (1) polycrystalline solidification analysis with a diffusive interface approach; and (2) subsequent stress analysis with the material interfaces, i.e., grain boundaries. Specifically, the PDM was used to tackle problems related to grain growth and solidification in a polycrystalline solid, as well as stress analysis of the resulting solid. This paper is organized as follows. First, the Taylor expansion and moving least-squares method used to develop the PDM are presented. The strong forms of the governing multiphase field equations for polycrystalline solidification and the equations of elastostatics for the stress analysis are discretized based on the particle difference scheme. Computational details and the simulation results for two-dimensional solidification problems are presented, followed by the accompanying stress analyses. The results from the PDM stress analyses are compared with results from the FEM on different grid sizes and nodal arrangements. Finally, a summary and concluding remarks are given.

Particle Difference Approximation

We provide a detailed derivation of the particle difference approximation in this section. One of the key ideas of the PDM is to use a standard Taylor series expansion with the moving least-squares approach to approximate field variables and their derivatives at the same time. For convenience, we start by defining mathematical notations. Let $\mathbf{x} = (x_1, \ldots, x_n)$ be an n-dimensional real vector and $\boldsymbol{\alpha} = (\alpha_1, \ldots, \alpha_n)$ be an n-tuple of nonnegative integers. The $\boldsymbol{\alpha}$th power of $\mathbf{x}$ is defined by

$$\mathbf{x}^{\boldsymbol{\alpha}} = x_1^{\alpha_1} x_2^{\alpha_2} \cdots x_n^{\alpha_n} \tag{1}$$

We define the $\boldsymbol{\alpha}$th derivative of a smooth function $f(\mathbf{x})$ with respect to $\mathbf{x}$ as

$$D^{\boldsymbol{\alpha}}_{\mathbf{x}} f(\mathbf{x}) = \frac{\partial^{|\boldsymbol{\alpha}|} f(\mathbf{x})}{\partial x_1^{\alpha_1} \partial x_2^{\alpha_2} \cdots \partial x_n^{\alpha_n}} \tag{2}$$

where $|\boldsymbol{\alpha}|$ = sum of all components of $\boldsymbol{\alpha}$, i.e., $|\boldsymbol{\alpha}| \equiv \sum_{i=1}^{n} \alpha_i$.

Upon neglecting higher-order terms in a Taylor series, the mth order polynomial for approximating a continuous function $u(\mathbf{x})$ at the local center $\bar{\mathbf{x}}$ can be expressed as

$$u(\mathbf{x}; \bar{\mathbf{x}}) = \sum_{|\boldsymbol{\alpha}| \le m} \frac{(\mathbf{x} - \bar{\mathbf{x}})^{\boldsymbol{\alpha}}}{\boldsymbol{\alpha}!} D^{\boldsymbol{\alpha}}_{\mathbf{x}} u(\bar{\mathbf{x}}) = \mathbf{p}_m^{\top}(\mathbf{x}; \bar{\mathbf{x}}) \mathbf{a}(\bar{\mathbf{x}}) \tag{3}$$

where $\boldsymbol{\alpha}!$ = factorial of $\boldsymbol{\alpha}$, i.e., $\boldsymbol{\alpha}! = \alpha_1! \cdots \alpha_n!$. The Taylor polynomial can be decomposed into the polynomial vector $\mathbf{p}_m^{\top}(\mathbf{x}; \bar{\mathbf{x}})$ and the derivative coefficient vector $\mathbf{a}(\bar{\mathbf{x}})$ computed at the local center. The polynomial vector takes the form

$$\mathbf{p}_m^{\top}(\mathbf{x}; \bar{\mathbf{x}}) = \left[\frac{\rho_1^{|\boldsymbol{\alpha}_1|}}{\boldsymbol{\alpha}_1!} \left(\frac{\mathbf{x} - \bar{\mathbf{x}}}{\rho_1} \right)^{\boldsymbol{\alpha}_1}, \ldots, \frac{\rho_L^{|\boldsymbol{\alpha}_L|}}{\boldsymbol{\alpha}_L!} \left(\frac{\mathbf{x} - \bar{\mathbf{x}}}{\rho_L} \right)^{\boldsymbol{\alpha}_L} \right] \tag{4}$$

where $\boldsymbol{\alpha} = n$-tuple of nonnegative integers; $L = (n+m)!/n!m!$ = number of the components of polynomial vector $\mathbf{p}_m^{\top}$; and $(\mathbf{x} - \bar{\mathbf{x}})^{\boldsymbol{\alpha}_i} = \boldsymbol{\alpha}_i$th power of $(\mathbf{x} - \bar{\mathbf{x}})$ defined by $(\mathbf{x} - \bar{\mathbf{x}})^{\boldsymbol{\alpha}_i} = (x_1 - \bar{x}_1)^{\alpha_{1i}} (x_2 - \bar{x}_2)^{\alpha_{2i}} \cdots (x_n - \bar{x}_n)^{\alpha_{ni}}$. The derivative coefficient vector can be defined as

$$\mathbf{a}^{\top}(\bar{\mathbf{x}}) = [D^{\boldsymbol{\alpha}_1}_{\mathbf{x}} u(\bar{\mathbf{x}}), \ldots, D^{\boldsymbol{\alpha}_L}_{\mathbf{x}} u(\bar{\mathbf{x}})] \tag{5}$$

which includes all of the derivatives for $u(\bar{\mathbf{x}})$ at the local center up to the $\boldsymbol{\alpha}_L$ th-order derivative.

The PDM uses the weight function $w[(x - x_I)/\rho_I]$ to define compact support which is nonzero over a neighborhood of x_I in order to generate set of sparse discrete equations for the discretized system of equations. In contrast to most meshfree methods, the PDM can use any function with a conical shape as the weight function. This is because no differentiability for the weight function is required in the PDM formulation. As long as the function is nonnegative and continuous, smoothness is not required. Most other meshfree methods, on the other hand, demand the differentiability of the weight function because the derivative of the approximation includes the derivative of the weight function. Nonsmooth weight functions were used previously (Kim and Kim 2003; Lee and Yoon 2004) in the framework of the meshfree point collocation method. It was also recognized that nonsmooth functions are preferable to smooth ones due to their resemblance to the Dirac delta function in the strongly formulated particle method through numerical experiments (Yoon and Song 2014b, c). Thus, in this study, we use the nondifferentiable functions

$$w_1\left(\frac{\mathbf{x} - \bar{\mathbf{x}}}{\rho_{\bar{\mathbf{x}}}} \right) = \left(1 - \left\| \frac{\mathbf{x} - \bar{\mathbf{x}}}{\rho_{\bar{\mathbf{x}}}} \right\| \right)^4 \tag{6}$$

and

$$w_2\left(\frac{\mathbf{x} - \bar{\mathbf{x}}}{\rho_{\bar{\mathbf{x}}}} \right) = \left(1 - \left\| \frac{\mathbf{x} - \bar{\mathbf{x}}}{\rho_{\bar{\mathbf{x}}}} \right\|^{1/2} \right)^2 \tag{7}$$

with a sharp peak and discontinuous derivatives. Fig. 1 illustrates an example of one-dimensional nonsmooth weight functions. The upper and lower bounds of the compact support sizes $\rho_{\bar{\mathbf{x}}}$ determine the computational efficiency and the invertibility of the moment matrix $\mathbf{M}$ which is subsequently described in Eq. (9), respectively. In this study, spatially varying continuous compact support function is constructed to evaluate the compact support size at each collocation point. To this end, a pseudocounting function is constructed based on the collocation density; details of the adopted computational algorithm were presented by Kim (2004).

Henceforth, we focus on the derivation of the PDM in two dimensions, but the derivation in one or three dimensions is much the same. In two dimensions, the Taylor polynomial for approximating a real function $u(\mathbf{x})$ at the local center $\bar{\mathbf{x}}$ can be expressed as in Eq. (3). The variables $\mathbf{x}$ and $\bar{\mathbf{x}}$ become vectors $\mathbf{x} = [x_1, x_2]^T$ and $\bar{\mathbf{x}} = [\bar{x}_1, \bar{x}_2]^T$.

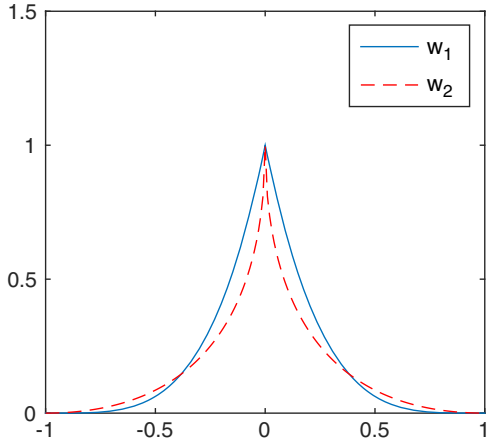

Fig. 1. Nonsmooth weight functions in one dimension.

Minimizing with respect to $\mathbf{a}(\bar{\mathbf{x}})$ the discrete form of the weighted, discrete L^2-norm given by

$$\mathbf{J} = \sum_{I=1}^{N} w\left(\frac{\mathbf{x}_I - \bar{\mathbf{x}}}{\rho_I}\right)[\mathbf{p}^\top(\mathbf{x}_I)\mathbf{a}(\bar{\mathbf{x}}) - u_I]^2 \tag{8}$$

yields

$$\mathbf{a}(\bar{\mathbf{x}}) = \begin{pmatrix} \mathbf{D}_{\mathbf{x}}^{\boldsymbol{\alpha}_1} u(\mathbf{x}) \\ \mathbf{D}_{\mathbf{x}}^{\boldsymbol{\alpha}_2} u(\mathbf{x}) \\ \vdots \\ \mathbf{D}_{\mathbf{x}}^{\boldsymbol{\alpha}_L} u(\mathbf{x}) \end{pmatrix} = \mathbf{M}^{-1}(\bar{\mathbf{x}})\mathbf{B}(\bar{\mathbf{x}})\mathbf{u}^\top \tag{9}$$

where matrices $\mathbf{M}$ and $\mathbf{B}$ are defined by

$$\mathbf{M}(\bar{\mathbf{x}}) = \sum_{I=1}^{N} w\left(\frac{\mathbf{x}_I - \bar{\mathbf{x}}}{\rho_I}\right)\mathbf{p}_m(\mathbf{x}_I;\bar{\mathbf{x}})\mathbf{p}_m^\top(\mathbf{x}_I;\bar{\mathbf{x}}) \tag{10}$$

$$\mathbf{B}(\bar{\mathbf{x}}) = \left[w\left(\frac{\mathbf{x}_1 - \bar{\mathbf{x}}}{\rho_1}\right)\mathbf{p}_m(\mathbf{x}_1;\bar{\mathbf{x}}), \ldots, w\left(\frac{\mathbf{x}_N - \bar{\mathbf{x}}}{\rho_N}\right)\mathbf{p}_m(\mathbf{x}_N;\bar{\mathbf{x}})\right] \tag{11}$$

Finally, substituting $\mathbf{x}$ for $\bar{\mathbf{x}}$ in Eq. (9) yields a general form of the particle derivative approximation as

$$\mathbf{D}_{\mathbf{x}}^{\boldsymbol{\alpha}_K} u(\mathbf{x}) = \sum_{I=1}^{N} \boldsymbol{\Phi}_I^{\boldsymbol{\alpha}_K}(\mathbf{x}) u_I \tag{12}$$

where $\boldsymbol{\alpha}_K = (\alpha_1, \alpha_2) =$ 2-tuple of nonnegative integers such as $\boldsymbol{\alpha}_1 = (0,0), \boldsymbol{\alpha}_2 = (1,0), \boldsymbol{\alpha}_3 = (0,1), \ldots, \boldsymbol{\alpha}_L = (0,m)$ for the m th-order polynomial vector $\mathbf{p}_m$; and $\boldsymbol{\Phi}_I^{\boldsymbol{\alpha}_K}(\mathbf{x}) = \boldsymbol{\alpha}_K$th derivative of the shape function at collocation point I which is further defined as

$$\boldsymbol{\Phi}_I^{\boldsymbol{\alpha}_K}(\mathbf{x}) = \mathbf{e}_{\boldsymbol{\alpha}_K}^\top \mathbf{M}^{-1}(\mathbf{x})\mathbf{B}(\mathbf{x}) \tag{13}$$

where $\mathbf{e}_{\alpha_K}^\top$ = Boolean vector in which 1 is placed at the $\boldsymbol{\alpha}$th slot in lexicographic order. The approximation of the solution and its derivative fields does not require the derivative of the weight function w. Thus, the continuity of the solution and its derivative fields do not rely on the continuity of the weight function.

Fig. 2 shows the shape functions and their first and second derivatives. Eq. (12) can be also expressed in matrix form as

$$\begin{pmatrix} \mathbf{D}_{\mathbf{x}}^{\boldsymbol{\alpha}_1} u(\mathbf{x}) \\ \mathbf{D}_{\mathbf{x}}^{\boldsymbol{\alpha}_2} u(\mathbf{x}) \\ \vdots \\ \mathbf{D}_{\mathbf{x}}^{\boldsymbol{\alpha}_L} u(\mathbf{x}) \end{pmatrix} = \begin{pmatrix} \boldsymbol{\Phi}_1^{\boldsymbol{\alpha}_1}(\mathbf{x}) & \boldsymbol{\Phi}_2^{\boldsymbol{\alpha}_1}(\mathbf{x}) & \cdots & \boldsymbol{\Phi}_N^{\boldsymbol{\alpha}_1}(\mathbf{x}) \\ \boldsymbol{\Phi}_1^{\boldsymbol{\alpha}_2}(\mathbf{x}) & \boldsymbol{\Phi}_2^{\boldsymbol{\alpha}_2}(\mathbf{x}) & \cdots & \boldsymbol{\Phi}_N^{\boldsymbol{\alpha}_2}(\mathbf{x}) \\ \vdots & \vdots & \ddots & \vdots \\ \boldsymbol{\Phi}_1^{\boldsymbol{\alpha}_L}(\mathbf{x}) & \boldsymbol{\Phi}_2^{\boldsymbol{\alpha}_L}(\mathbf{x}) & \cdots & \boldsymbol{\Phi}_N^{\boldsymbol{\alpha}_L}(\mathbf{x}) \end{pmatrix} \begin{pmatrix} u_1 \\ u_2 \\ \vdots \\ u_N \end{pmatrix} \tag{14}$$

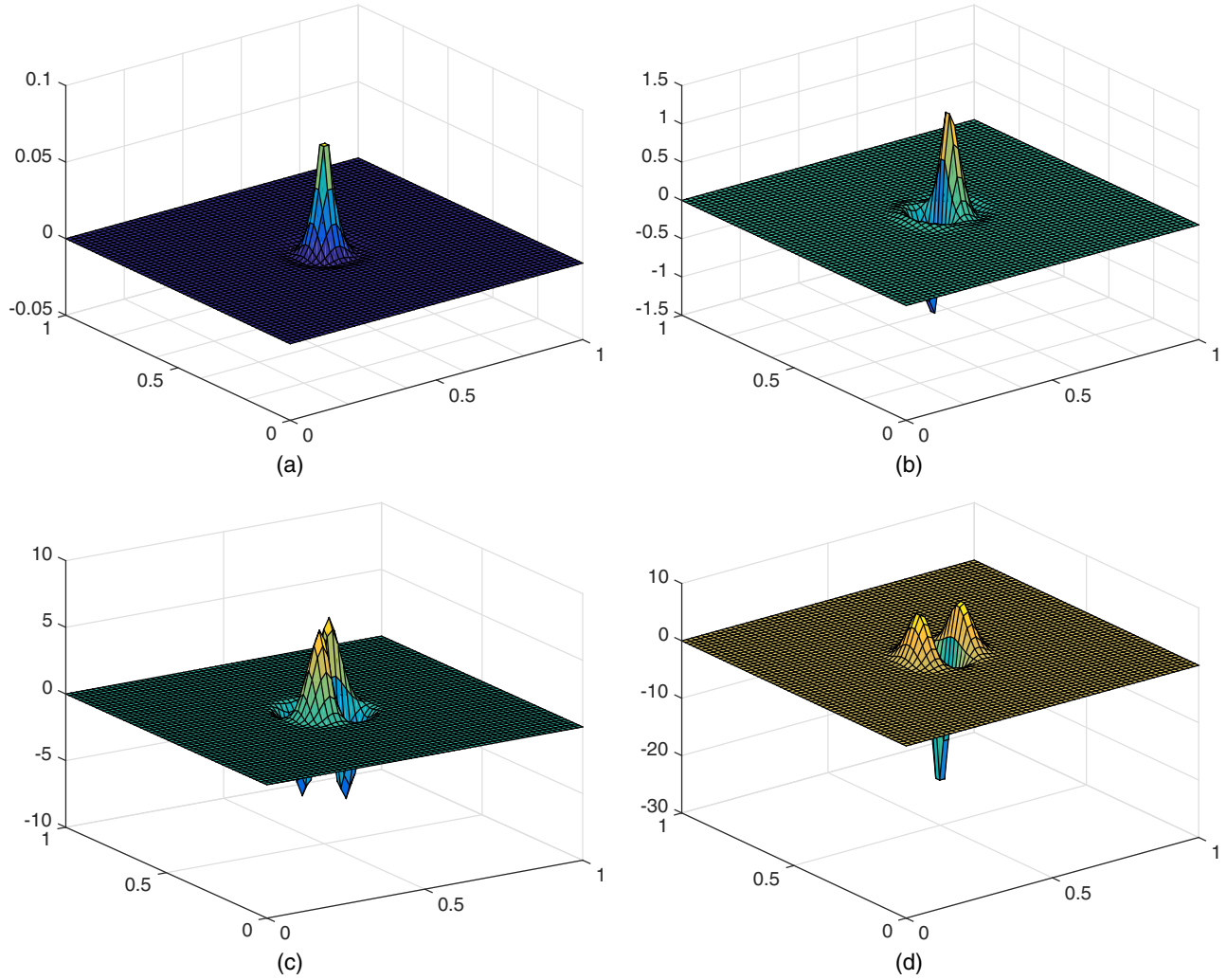

Fig. 2. Two-dimensional shape functions and their derivatives: (a) $\Phi^{(0,0)}(\mathbf{x})$; (b) $\Phi^{(1,0)}(\mathbf{x})$; (c) $\Phi^{(1,1)}(\mathbf{x})$; and (d) $\Phi^{(2,0)}(\mathbf{x})$.

J. Eng. Mech., 2019, 145(10): 04019082

We further detail the previously described particle difference approximation scheme for the specific cases of the linear and quadratic orders of the polynomial vector $\mathbf{p}$. In two dimensions, the Taylor polynomial, i.e., Eq. (3) approximating a function $u(\mathbf{x})$ at a local center $\bar{\mathbf{x}} = [\bar{x}_1, \bar{x}_2]$, can be written

$$u(\mathbf{x}) = u(\bar{\mathbf{x}}) + D_{\mathbf{x}}^{(1,0)} u(\bar{\mathbf{x}})(x_1 - \bar{x}_1) + D_{\mathbf{x}}^{(0,1)} u(\bar{\mathbf{x}})(x_2 - \bar{x}_2) \quad (15)$$

for the linear case ($m = 1$) and

$$u(\mathbf{x}) = u(\bar{\mathbf{x}}) + D_{\mathbf{x}}^{(1,0)} u(\bar{\mathbf{x}})(x_1 - \bar{x}_1) + D_{\mathbf{x}}^{(0,1)} u(\bar{\mathbf{x}})(x_2 - \bar{x}_2) + D_{\mathbf{x}}^{(2,0)} u(\bar{\mathbf{x}}) \frac{(x_1 - \bar{x}_1)^2}{2!} + D_{\mathbf{x}}^{(1,1)} u(\bar{\mathbf{x}})(x_1 - \bar{x}_1)(x_2 - \bar{x}_2) + D_{\mathbf{x}}^{(0,2)} u(\bar{\mathbf{x}}) \frac{(x_2 - \bar{x}_2)^2}{2!} \quad (16)$$

for the quadratic case ($m = 2$). The $\mathbf{p}$ vectors are given by

$$\mathbf{p}_1^\top(\mathbf{x}; \bar{\mathbf{x}}) = \left[1 \quad \frac{\rho}{1!}\left(\frac{x_1 - \bar{x}_1}{\rho}\right)^1 \quad \frac{\rho}{1!}\left(\frac{x_2 - \bar{x}_2}{\rho}\right)^1 \right] \quad (17)$$

for the linear case and

$$\mathbf{p}_2^\top(\mathbf{x}; \bar{\mathbf{x}}) = \left[1 \quad \frac{\rho}{1!}\left(\frac{x_1 - \bar{x}_1}{\rho}\right)^1 \quad \frac{\rho}{1!}\left(\frac{x_2 - \bar{x}_2}{\rho}\right)^1 \quad \frac{\rho^2}{2!}\left(\frac{x_1 - \bar{x}_1}{\rho}\right)^2 \quad \frac{\rho^2}{1!1!}\left(\frac{(x_1 - \bar{x}_1)(x_2 - \bar{x}_2)}{\rho^2}\right) \quad \frac{\rho^2}{2!}\left(\frac{x_2 - \bar{x}_2}{\rho}\right)^2 \right] \quad (18)$$

for the quadratic case. The matrices $\mathbf{M}$ and $\mathbf{B}$ can be expanded as

$$\mathbf{M}(\bar{\mathbf{x}}) = \sum_{I=1}^{N} w\left(\frac{\mathbf{x}_I - \bar{\mathbf{x}}}{\rho_{\bar{\mathbf{x}}}}\right) \mathbf{p}_1(\mathbf{x}_I; \bar{\mathbf{x}}) \mathbf{p}_1^\top(\mathbf{x}_I; \bar{\mathbf{x}}) = \sum_{I=1}^{N} w\left(\frac{\mathbf{x}_I - \bar{\mathbf{x}}}{\rho_{\bar{\mathbf{x}}}}\right) \begin{bmatrix} 1 & d_{I1} & d_{I2} \\ I1 & (d_{I1})^2 & d_{I1} d_{I2} \\ d_{I2} & d_{I1} d_{I2} & (d_{I2})^2 \end{bmatrix} \quad (19)$$

for the linear case and

$$\mathbf{M}(\bar{\mathbf{x}}) = \sum_{I=1}^{N} w\left(\frac{\mathbf{x}_I - \bar{\mathbf{x}}}{\rho_{\bar{\mathbf{x}}}}\right) \mathbf{p}_2(\mathbf{x}_I; \bar{\mathbf{x}}) \mathbf{p}_2^\top(\mathbf{x}_I; \bar{\mathbf{x}}) = \sum_{I=1}^{N} w\left(\frac{\mathbf{x}_I - \bar{\mathbf{x}}}{\rho_{\bar{\mathbf{x}}}}\right) \begin{bmatrix} 1 & d_{I1} & d_{I2} & d_{I1}^2/2 & d_{I1} d_{I2} & d_{I2}^2/2 \\ d_{I1} & d_{I1}^2 & d_{I1} d_{I2} & d_{I1}^3/2 & d_{I1}^2 d_{I2} & d_{I1} d_{I2}^2/2 \\ d_{I2} & d_{I1} d_{I2} & d_{I2}^2 & d_{I1}^2 d_{I2}/2 & d_{I1} d_{I2}^2 & d_{I2}^3/2 \\ d_{I1}^2/2 & d_{I1}^3/2 & d_{I1}^2 d_{I2}/2 & d_{I1}^4/2 & d_{I1}^3 d_{I2}/2 & d_{I1}^2 d_{I2}^2/4 \\ d_{I1} d_{I2} & d_{I1}^2 d_{I2} & d_{I1} d_{I2}^2 & d_{I1}^3 d_{I2}/2 & d_{I1}^2 d_{I2}^2 & d_{I1} d_{I2}^3/2 \\ d_{I2}^2/2 & d_{I1} d_{I2}^2/2 & d_{I2}^3/2 & d_{I1}^2 d_{I2}^2/4 & d_{I1} d_{I2}^3/2 & d_{I1}^2 d_{I2}^2/4 \end{bmatrix} \quad (20)$$

for the quadratic case. In Eqs. (19) and (20), $d_{Ii} = x_{Ii} - \bar{x}_i$ for $i = 1, 2$ with $\mathbf{x}_I = [x_{I1}, x_{I2}]$. The derivative coefficient vectors for the linear and quadratic cases can be respectively defined as

$$\mathbf{D}_{\mathbf{x}}^{\boldsymbol{\alpha}} u(\mathbf{x}) = [u(\mathbf{x}), D_{\mathbf{x}}^{(1,0)} u(\mathbf{x}), D_{\mathbf{x}}^{(0,1)} u(\mathbf{x})] \quad (21)$$

and

$$\mathbf{D}_{\mathbf{x}}^{\boldsymbol{\alpha}} u(\mathbf{x}) = \left[u(\mathbf{x}), D_{\mathbf{x}}^{(1,0)} u(\mathbf{x}), D_{\mathbf{x}}^{(0,1)} u(\mathbf{x}), D_{\mathbf{x}}^{(2,0)} u(\mathbf{x}), D_{\mathbf{x}}^{(1,1)} u(\mathbf{x}), D_{\mathbf{x}}^{(0,2)} u(\mathbf{x}) \right] \quad (22)$$

Discretization of Governing Equations

Polycrystalline Solidification

Polycrystalline solidification in a material is described with a multiphase field model (Fan and Chen 1997). The phases refer to crystal orientations of grains within the domain, each corresponding to a multiphase field order parameter $\varphi_i \in [0, 1]$ where $i = 1, 2, \ldots, p$, where p is the total number of grains considered in the solidification analysis. In addition, φ_0 is assigned to model the liquid phase of the material. At each spatial point $\mathbf{x}$ in the solidifying body, it is assumed that the liquid phase and differently-oriented solid phases are presented so that $\sum_{i=0}^{p} \varphi_i(\mathbf{x}) = 1$. For example, if a material point $\mathbf{x}$ in the domain is molten metal, φ_0 will be at or near unity, and the other phase field parameters, i.e., $\varphi_1, \ldots, \varphi_p$ will be at or near zero. Fig. 3 is a schematic of microstructure described with the multiphase field order parameters.

The multiphase field model is based on the diffuse interface approach. In other words, at each diffusive interface, i.e., grain boundary, the order parameters corresponding to either grain should smoothly vary between 0 and 1 within a very narrow region. Based on thermodynamic considerations (Fan and Chen 1997; Allen and Cahn 1979), the spatial gradients of these diffusive interfaces drive the temporal evolution of the grain boundaries. These considerations lead to the following diffusive-type evolution equation to model the polycrystalline solidification process:

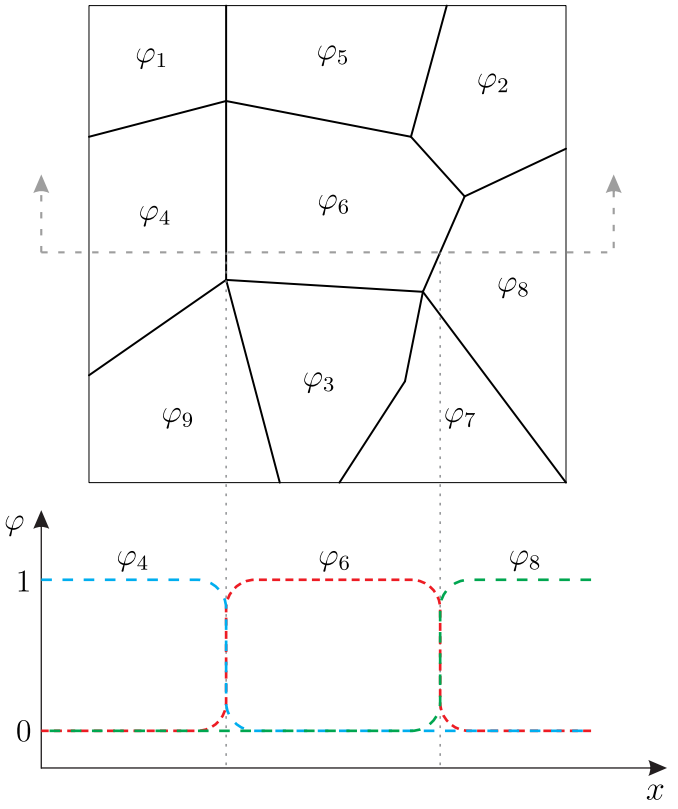

Fig. 3. Schematic of a polycrystalline microstructure described with the multiphase field order parameters $\varphi_i \in [0, 1]$, where $i = 1, \ldots, 9$.

$$\frac{\partial \varphi_i(\boldsymbol{x}, t)}{\partial t} = -M_i \frac{\delta F}{\delta \varphi_i(\boldsymbol{x}, t)} \tag{23}$$

where $\varphi_i = i$th phase field order parameter; M_i = interface mobility constant; and F is a functional representing the total free energy of a system defined by

$$F[\varphi_i, \nabla\varphi_i] = \int_V [f_0(\varphi_1(\mathbf{x}), \varphi_2(\mathbf{x}), \ldots, \varphi_p(\mathbf{x})) + \sum_{i=1}^{p} \frac{\kappa_i}{2} (\nabla\varphi_i(\mathbf{x}))^2] dV \tag{24}$$

where κ_i = gradient energy coefficient of grain i; and f_0 = local free energy density given by

$$f_0(\varphi_1, \varphi_2, \ldots, \varphi_p) = \sum_{i=1}^{p} \left(-\frac{\alpha}{2}\varphi_i^2 + \frac{\beta}{4}\varphi_i^4 \right) + \gamma \sum_{i=1}^{p} \sum_{j \neq i}^{p} \varphi_i^2 \varphi_j^2 \tag{25}$$

where α, β, and γ = material parameters required to be determined experimentally.

By taking the first variational derivative of Eq. (23) with Eqs. (24) and (25), the governing equation for polycrystalline solidification is rewritten

$$\frac{\partial \varphi_i}{\partial t} = -M_i \left(-\alpha\varphi_i + \beta\varphi_i^3 + 2\gamma\varphi_i \sum_{j \neq i}^{p} \varphi_j^2 - \kappa_i \nabla^2 \varphi_i \right) \quad \text{where } i = 1, 2, \ldots, p \tag{26}$$

For the time integration of Eq. (26), we adopted the forward Euler scheme by

$$\frac{\varphi_i^{n+1} - \varphi_i^n}{\Delta t} = -M_i \left(-\alpha\varphi_i^n + \beta(\varphi_i^n)^3 + 2\gamma\varphi_i^n \sum_{j \neq i}^{p} (\varphi_j^n)^2 - \kappa_i \nabla^2 \varphi_i^n \right) \quad \text{where } i = 1, 2, \ldots, p \tag{27}$$

where Δt = time integration step size; the superscripts on the phase field order parameter φ indicate the indices for the time steps; and operator ∇^2 denotes a discrete form of the Laplacian operator. Further discretization of Eq. (27) with the PDM yields the final system of equations given by

$$\sum_{I=1}^{N} L_I^{\Omega}(\mathbf{X}) \varphi_I^{(n+1)} = F_{\varphi}^{\Omega}(\mathbf{X}) \tag{28}$$

where subscript I indicates the nodal index. The discrete differential operator $L_I^{\Omega}(\mathbf{X})$ is written

$$L_I^{\Omega}(\mathbf{X}) = \boldsymbol{\Phi}_I^{(0,0)}(\mathbf{X}) \tag{29}$$

The generalized force $F_{\varphi}^{\Omega}(\mathbf{X})$ on the right-hand side of Eq. (28) takes the form

$$\begin{aligned} F_{\varphi}^{\Omega}(\mathbf{X}) = & \sum_{I=1}^{N} \boldsymbol{\Phi}_I^{(0,0)}(\mathbf{X}) \varphi_{iI}^n \\ & + \Delta t M_i \Bigg\{ \alpha \sum_{I=1}^{N} \boldsymbol{\Phi}_I^{(0,0)}(\mathbf{X}) \varphi_{iI}^n - \beta \sum_{I=1}^{N} (\boldsymbol{\Phi}_I^{(0,0)}(\mathbf{X})(\varphi_{iI}^n))^3 \\ & - 2\gamma \sum_{I=1}^{N} \boldsymbol{\Phi}_I^{(0,0)}(\mathbf{X}) \varphi_{iI}^n \left(\sum_{j \neq i}^{p} \sum_{I=1}^{N} (\boldsymbol{\Phi}_I^{(0,0)}(\mathbf{X})(\varphi_{jI}^n))^2 \right) \\ & + \kappa_i \sum_{I=1}^{N} (\boldsymbol{\Phi}_I^{(2,0)}(\mathbf{X}) + \boldsymbol{\Phi}_I^{(0,2)}(\mathbf{X})) \sum_{I=1}^{N} \boldsymbol{\Phi}_I^{(0,0)}(\mathbf{X}) \varphi_{iI}^n \Bigg\} \end{aligned} \tag{30}$$

Elastostatics for Polycrystalline Stress Analysis

In addition to polycrystalline solidification, we also sought to determine the effect of mechanical loading on solidified polycrystalline materials. To this end, the two-dimensional linear elastostatics problem was considered upon completion of the grain solidification prediction. This elastostatics problem for a domain Ω bounded by Γ (Fig. 4) takes the form

$$\text{div}\boldsymbol{\sigma} + \mathbf{b} = 0 \quad \text{in } \Omega \tag{31}$$

where $\boldsymbol{\sigma}$ = Cauchy stress tensor; $\mathbf{u}$ = displacement field; and $\mathbf{b}$ = body force vector. The Dirichlet and Neumann boundary conditions are given by

$$\mathbf{u} = \bar{\mathbf{u}} \quad \text{on } \Gamma_u \tag{32a}$$

$$\boldsymbol{\sigma}\mathbf{n} = \bar{\mathbf{t}} \quad \text{on } \Gamma_t \tag{32b}$$

where $\mathbf{n}$ = outward unit normal vector on Γ_t; $\Gamma = \Gamma_u \cup \Gamma_t$; and $\Gamma_u \cap \Gamma_t = \emptyset$.

The constitutive equation for a linear isotropic elastic material is given by

$$\sigma = \lambda \text{tr}(\boldsymbol{\varepsilon})\mathbf{1} + 2\mu\boldsymbol{\varepsilon} \tag{33}$$

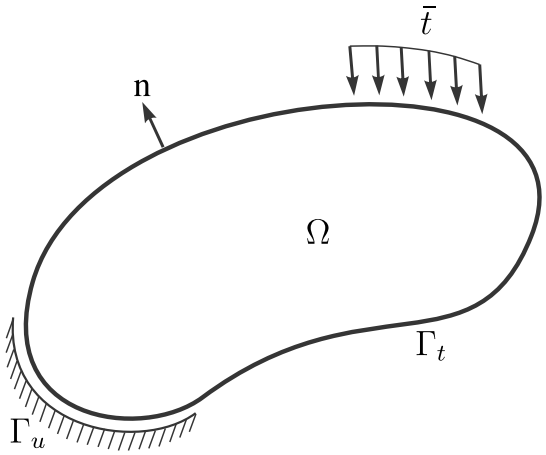

Fig. 4. Two-dimensional body Ω with the outward unit normal vector, i.e., $\mathbf{n}$.

where λ and μ = Lamé constants; and $\mathbf{1}$ = second-order identity tensor. For the plane stress condition

$$\lambda = \frac{\nu E}{1-\nu^2}$$
$$\mu = G = \frac{E}{2(1+\nu)} \tag{34}$$

where E = Young's modulus; G = shear modulus; and ν = Poisson's ratio. For a linear isotropic elastic material, based on the assumption of small displacement and strain, the Cauchy infinitesimal strain tensor is defined by $\boldsymbol{\varepsilon} = (\nabla \mathbf{u} + (\nabla \mathbf{u})^{\top})/2$. Substituting Eq. (33) into Eq. (31) yields the governing equation

$$\text{div}[\lambda \text{tr}(\boldsymbol{\varepsilon})\mathbf{1} + 2\mu\boldsymbol{\varepsilon}] + \mathbf{b} = 0 \quad \text{in } \Omega \tag{35}$$

We discretize the governing equation with the PDM. For convenience, we define $\Lambda = \Lambda_i \cup \Lambda_d \cup \Lambda_n$, where Λ_i, Λ_d, and Λ_n are sets of interior nodes, Dirichlet boundary nodes, and Neumann boundary nodes, respectively. To facilitate further expression for the discretized governing equation with the PDM, Eq. (35) is rewritten

$$\lambda u_{k,ki} + \mu(u_{i,jj} + u_{j,ji}) + b_i = 0 \quad \text{in } \Omega \tag{36}$$

for a homogeneous material, i.e., material properties form constant fields. However, if the material properties have a spatial variation, i.e., bimaterial or polycrystalline materials, Eq. (35) should be further developed to include spatial derivatives of the material property fields

$$\lambda_{,i} u_{k,k} + \mu_{,j}(u_{i,j} + u_{j,i}) + \lambda u_{k,ki} + \mu(u_{i,jj} + u_{j,ij}) + b_i = 0 \quad \text{in } \Omega \tag{37}$$

where $i, j = 1, 2$ in two dimensions and the repeated subscript follows the summation convention. Another elegant approach for modeling material interface with a variational formulation and a double-grid method was proposed by Chen et al. (2004). Substituting Eq. (12) into Eq. (37) yields the discrete form of equations which are given by

$$\begin{aligned}
&\sum_{I=1}^{N}[(\lambda+2\mu)\boldsymbol{\Phi}_I^{(2,0)}(\mathbf{x}_J)u_{1I} + \mu\boldsymbol{\Phi}_I^{(0,2)}(\mathbf{x}_J)u_{1I} \\
&\quad + (\lambda+\mu)\boldsymbol{\Phi}_I^{(1,1)}(\mathbf{x}_J)u_{2I} + \boldsymbol{\Phi}_I^{(1,0)}(\mathbf{x}_J)\lambda(\boldsymbol{\Phi}_I^{(1,0)}(\mathbf{x}_J)u_{1I} \\
&\quad + \boldsymbol{\Phi}_I^{(0,1)}(\mathbf{x}_J)u_{2I}) + \boldsymbol{\Phi}_I^{(1,0)}(\mathbf{x}_J)\mu(\boldsymbol{\Phi}_I^{(0,1)}(\mathbf{x}_J)u_{1I} \\
&\quad + \boldsymbol{\Phi}_I^{(1,0)}(\mathbf{x}_J)u_{2I})) + \boldsymbol{\Phi}_I^{(1,0)}(\mathbf{x}_J)\mu(2\boldsymbol{\Phi}_I^{(1,0)}(\mathbf{x}_J)u_{1I}] = -b_1(\mathbf{x}_J) \\
&\sum_{I=1}^{N}[(\lambda+2\mu)\boldsymbol{\Phi}_I^{(0,2)}(\mathbf{x}_J)u_{2I} + \mu\boldsymbol{\Phi}_I^{(2,0)}(\mathbf{x}_J)u_{2I} \\
&\quad + (\lambda+\mu)\boldsymbol{\Phi}_I^{(1,1)}(\mathbf{x}_J)u_{1I} + \boldsymbol{\Phi}_I^{(0,1)}(\mathbf{x}_J)\lambda(\boldsymbol{\Phi}_I^{(1,0)}(\mathbf{x}_J)u_{1I} \\
&\quad + \boldsymbol{\Phi}_I^{(0,1)}(\mathbf{x}_J)u_{2I}) + \boldsymbol{\Phi}_I^{(1,0)}(\mathbf{x}_J)\mu(\boldsymbol{\Phi}_I^{(0,1)}(\mathbf{x}_J)u_{1I} \\
&\quad + \boldsymbol{\Phi}_I^{(1,0)}(\mathbf{x}_J)u_{2I})) + \boldsymbol{\Phi}_I^{(0,1)}(\mathbf{x}_J)\mu(2\boldsymbol{\Phi}_I^{(0,1)}(\mathbf{x}_J)u_{2I}] = -b_2(\mathbf{x}_J)
\end{aligned} \tag{38}$$

for the interior nodes $\mathbf{x}_J \in \Lambda_i$. In contrast to Eq. (38), if the body consists of a homogeneous material, the spatial derivatives of λ and μ vanish, and Eq. (38) is reduced to

$$\begin{aligned}
&\sum_{I=1}^{N}[(\lambda+2\mu)\boldsymbol{\Phi}_I^{(2,0)}(\mathbf{x}_J)u_{1I} + \mu\boldsymbol{\Phi}_I^{(0,2)}(\mathbf{x}_J)u_{1I} \\
&\quad + (\lambda+\mu)\boldsymbol{\Phi}_I^{(1,1)}(\mathbf{x}_J)u_{2I}] = -b_1(\mathbf{x}_J) \\
&\sum_{I=1}^{N}[(\lambda+\mu)\boldsymbol{\Phi}_I^{(1,1)}(\mathbf{x}_J)u_{1I} + \mu\boldsymbol{\Phi}_I^{(2,0)}(\mathbf{x}_J)u_{2I} \\
&\quad + (\lambda+2\mu)\boldsymbol{\Phi}_I^{(0,2)}(\mathbf{x}_J)u_{2I}] = -b_2(\mathbf{x}_J)
\end{aligned} \tag{39}$$

for the interior nodes $\mathbf{x}_J \in \Lambda_i$. The discrete form of the Dirichlet boundary condition can be obtained by substituting Eq. (12) into Eq. (32*a*) as

$$\begin{aligned}
\sum_{I=1}^{N}\boldsymbol{\Phi}_I^{(0,0)}(\mathbf{x}_J)u_{1I} &= \bar{u}_{1I}(\mathbf{x}_J) \\
\sum_{I=1}^{N}\boldsymbol{\Phi}_I^{(0,0)}(\mathbf{x}_J)u_{2I} &= \bar{u}_{2I}(\mathbf{x}_J)
\end{aligned} \tag{40}$$

for the Dirichlet boundary nodes $\mathbf{x}_J \in \Lambda_d$. Similarly, for the discretization of the Neumman boundary condition, i.e., Eq. (32*b*), substituting Eq. (33) into Eq. (32*b*) yields

$$2\mu\mathbf{n}\cdot\boldsymbol{\varepsilon} + \lambda\mathbf{n}\cdot\mathbf{1}(\text{div}\mathbf{u}) = \bar{\mathbf{t}} \quad \text{on } \Gamma_t \tag{41}$$

which, in Cartesian components, has the equivalent form

$$\mu(u_{i,j} + u_{j,i})n_j + \lambda\delta_{ij}n_j(u_{k,k}) = \bar{t}_i \quad \text{on } \Gamma_t \tag{42}$$

where δ_{ij} = Kronecker delta. For the discretization of Eq. (42) with the PDM, substituting Eq. (12) into Eq. (42) results in

$$\begin{aligned}
&\sum_{I=1}^{N}\{[(\lambda+2\mu)\boldsymbol{\Phi}_I^{(1,0)}(\mathbf{x}_J)n_1 + \mu\boldsymbol{\Phi}_I^{(0,1)}(\mathbf{x}_J)n_2]u_{1I} \\
&\quad + [\lambda\boldsymbol{\Phi}_{IJ}^{(0,1)}(\mathbf{x}_J)n_1 + \mu\boldsymbol{\Phi}_{IJ}^{(1,0)}(\mathbf{x}_J)n_2]u_{2I}\} = \bar{t}_1(\mathbf{x}_J) \\
&\sum_{I=1}^{N}\{[\mu\boldsymbol{\Phi}_I^{(0,1)}(\mathbf{x}_J)n_1 + \lambda\boldsymbol{\Phi}_I^{(1,0)}(\mathbf{x}_J)n_2]u_{1I} \\
&\quad + [(\lambda+2\mu)\boldsymbol{\Phi}_I^{(0,1)}(\mathbf{x}_J)n_2 + \mu\boldsymbol{\Phi}_I^{(1,0)}(\mathbf{x}_J)n_1]u_{2I}\} = \bar{t}_2(\mathbf{x}_J)
\end{aligned} \tag{43}$$

for the Neumman boundary nodes $\mathbf{x}_J \in \Lambda_n$.

J. Eng. Mech., 2019, 145(10): 04019082

Upon assembling Eqs. (38), (40), and (43), we obtain the linear algebraic system of equations for elastostatic analysis in the form of $\mathbf{Lu} = \mathbf{f}$, where $\mathbf{L}$ is the sparse matrix consisting of assembled derivative coefficient of the PDM based on Eqs. (38), (40), and (43).

Numerical Study

The performance of the PDM was examined via polycrystalline structure prediction and stress analysis. We began by obtaining a steady-state polycrystalline structure from the solidification using the multiphase field model. Then, upon considering the polycrystalline structure as a computational domain, an elastostatic stress analysis was performed. This section considers polycrystalline grain growth and stress analysis for the following three cases: (1) 5 grains, (2) 36 grains, and (3) 30 grains with 6 rigid inclusions.

Polycrystalline Solidification with Phase Field Model

We obtained two-dimensional polycrystalline structures for the aforementioned three different cases using the multiphase field

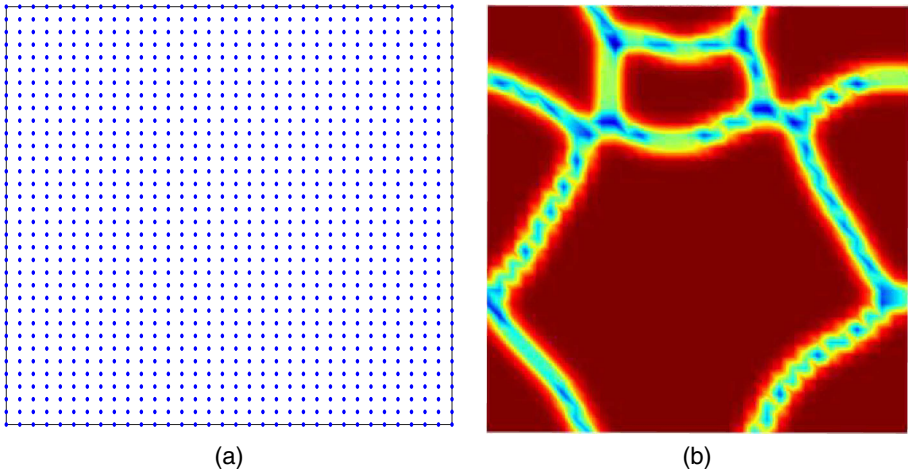

Fig. 5. (a) Discretization of polycrystalline analysis domain with 1,156 collocation points; and (b) steady-state polycrystalline structure with 5 orientation variables.

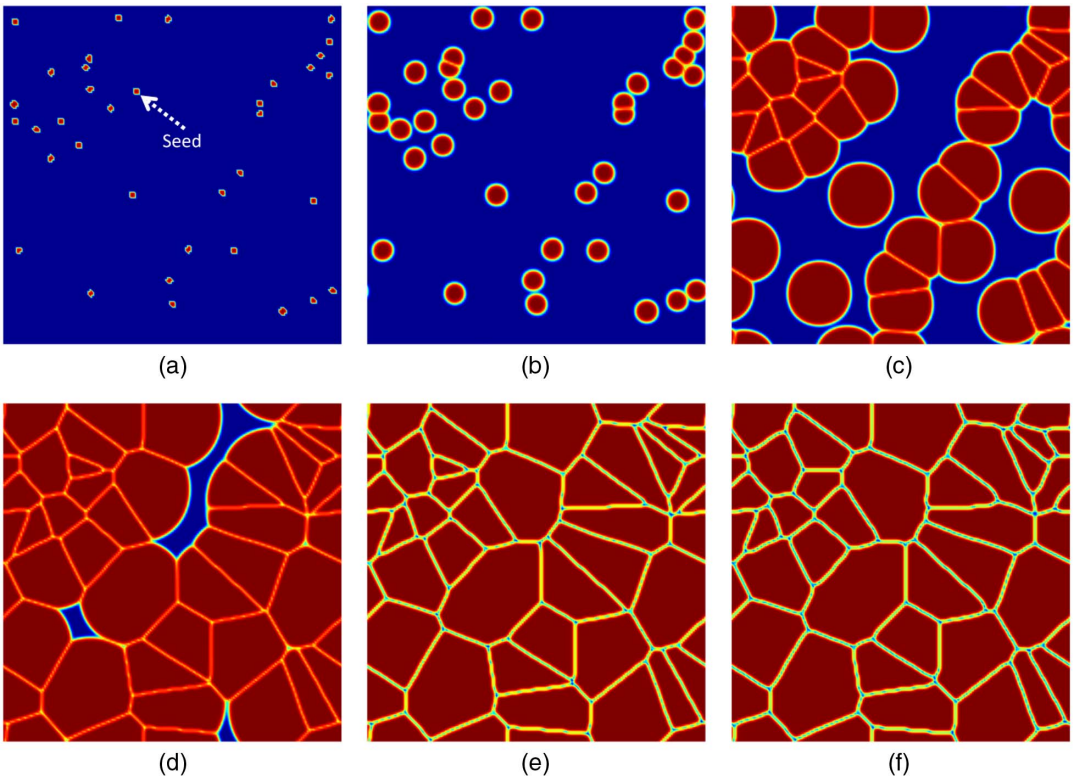

Fig. 6. Evolution of polycrystalline structure with 36 grains shown at simulation time: (a) $t = 0$ (initial state); (b) $t = 50\Delta t$; (c) $t = 100\Delta t$; (d) $t = 150\Delta t$; (e) $t = 200\Delta t$; and (f) $t = 8000\Delta t$ (final state).

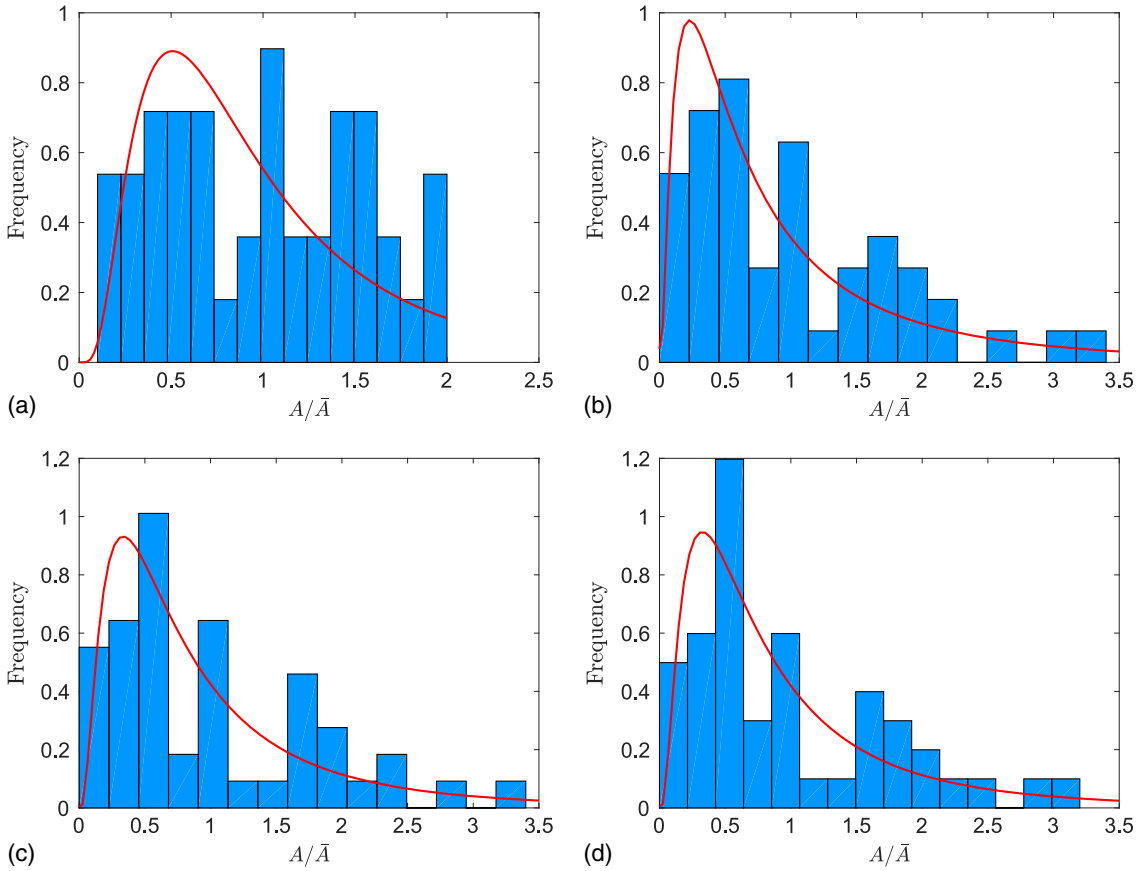

Fig. 7. Evolution of area distribution for polycrystalline solidification analysis with 36 grains, showing histograms with log-normal function at time step: (a) $t = 100\Delta t$; (b) $t = 150\Delta t$; (c) $t = 200\Delta t$; and (d) $t = 8000\Delta t$.

model, i.e., Eq. (26) with the PDM. The computational domain was chosen to be an $L \times H$ rectangle. Unless otherwise specified, periodic boundary conditions were applied in all directions of the computational domain for the polycrystalline solidification analysis with the multiphase file model. The simulation parameters for the phase field model were nondimensionalized as in Fan and Chen (1997), and the kinetic parameters for the solidification analysis were assumed to be $\alpha = 1.0$, $\beta = 1.0$, $\gamma = 1.0$, $\kappa_i = 2.0$, and $M_i = 1.0$ for $i = 1$–p, where p is the total number of phase field order parameters, i.e., the total number of initial grains within the computational

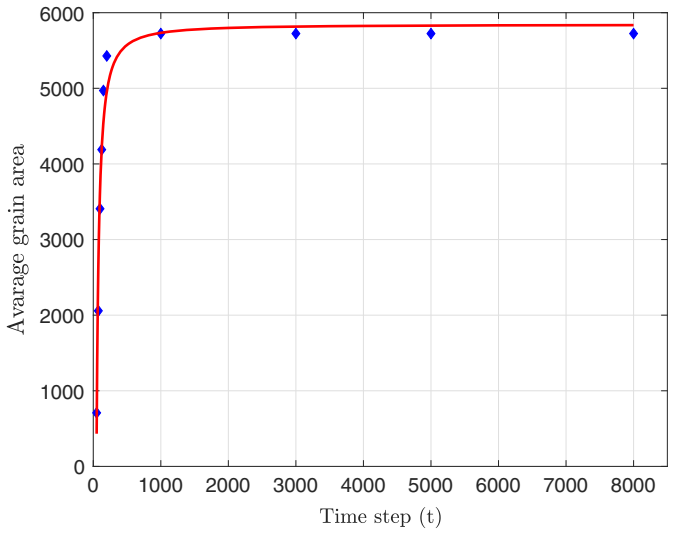

Fig. 8. Evolution of average grain area for polycrystalline structure with 36 grains.

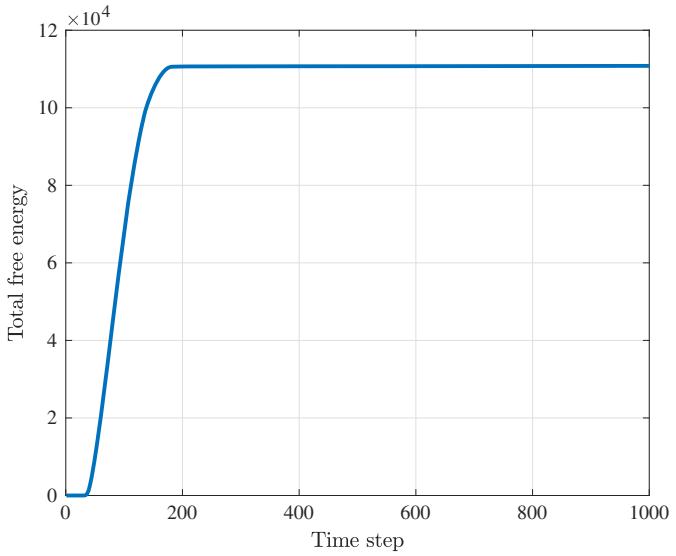

Fig. 9. Evolution of the total free energy for polycrystalline structure with 36 grains.

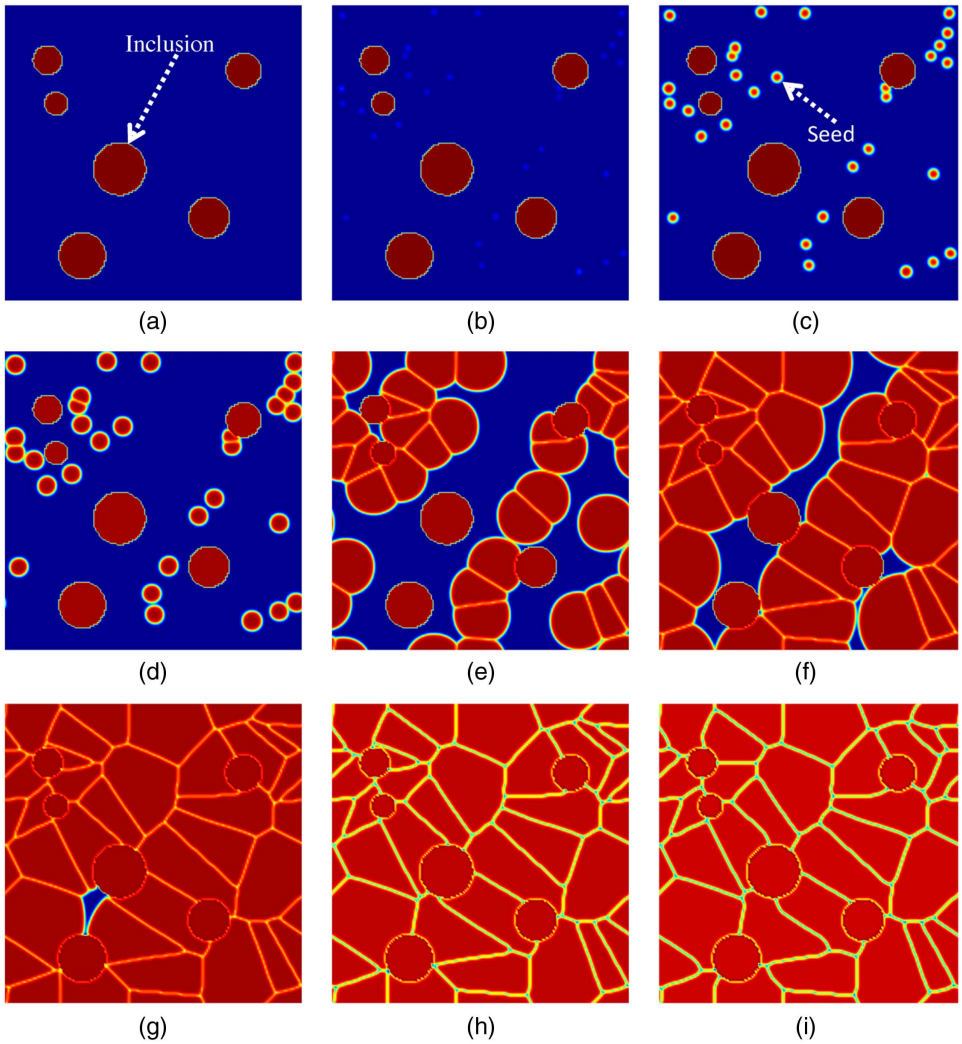

Fig. 10. Evolution of polycrystalline structure with 30 grains and 6 inclusions shown at simulation time: (a) $t = 0$ (initial state); (b) $t = 30\Delta t$; (c) $t = 40\Delta t$; (d) $t = 50\Delta t$; (e) $t = 100\Delta t$; (f) $t = 150\Delta t$; (g) $t = 200\Delta t$; (h) $t = 300\Delta t$; and (i) $t = 5000\Delta t$ (final state).

domain. An explicit time integration scheme was adopted with time step size $\Delta t = 0.25$, which was sufficiently small for stable time integration. To help decide when to terminate the phase field model analysis, the free energy of the phase field model was monitored so that the phase field simulation stopped when the computed free-energy of the phase field model reached a steady-state.

Fig. 5 shows the initial discretization of the computational domain and the final configuration of the polycrystalline structure for the phase field model analysis with five grains. This polycrystalline structure was obtained with the uniformly distributed arrangement of 1,156 collocation points shown in Fig. 5(a). Although the predicted morphology of the polycrystalline structure has a certain resemblance to actual observed polycrystalline materials, the predicted polycrystalline structure suffers from a highly irregular distribution of the grain sizes, and the curved grain boundaries that are uncommon in observed polycrystalline materials.

However, such an irregularity in the distribution of grain sizes can be alleviated when we consider a large enough number of grains for the solidification analysis. For example, in contrast to the previous example, which considered only 5 grains, the polycrystalline structure predicted with 36 grains growth had a more uniform distribution of the grain sizes with more straight grain boundaries. The 36-grain simulation used a total of 29,241 collocation points. The polycrystalline structure obtained from the evolution of the phase field model with 36 orientation variables is shown in Fig. 6. Fig. 6(a) shows the initial state as an arrangement of circular seed grains generated from a Poisson random seeding algorithm (Simmons et al. 2000), and Fig. 6(f) shows the final configuration

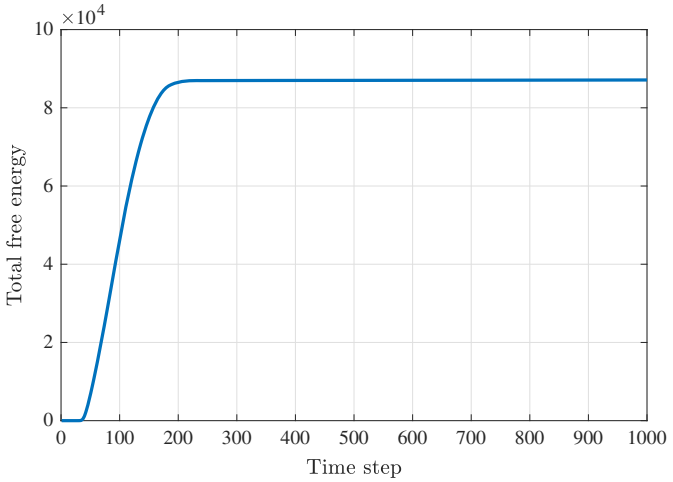

Fig. 11. Evolution of the total free energy for polycrystalline structure with 30 grains and 6 inclusions.

of the steady-state polycrystalline structure. Interestingly, between Figs. 6(e and f), although the polycrystalline morphology seems to have reached a steady state, some subtle changes occurred after $t = 200\Delta t$, i.e., Fig. 6(e). For example, in the upper left corner of the domain, a cluster of four grains with a small grain in the middle [Fig. 6(e)] became a cluster of three grains when the middle cluster disappeared [Fig. 6(f)]. Subtle changes such as this help explain why it is important to monitor the free energy of the system

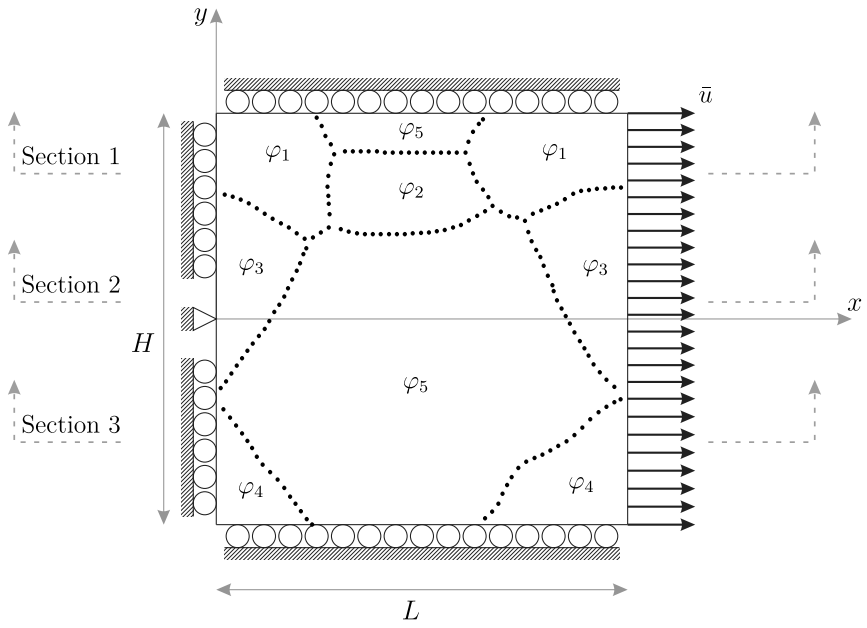

Fig. 12. Polycrystalline structure with five grains with boundary conditions, including the prescribed displacement at the right side.

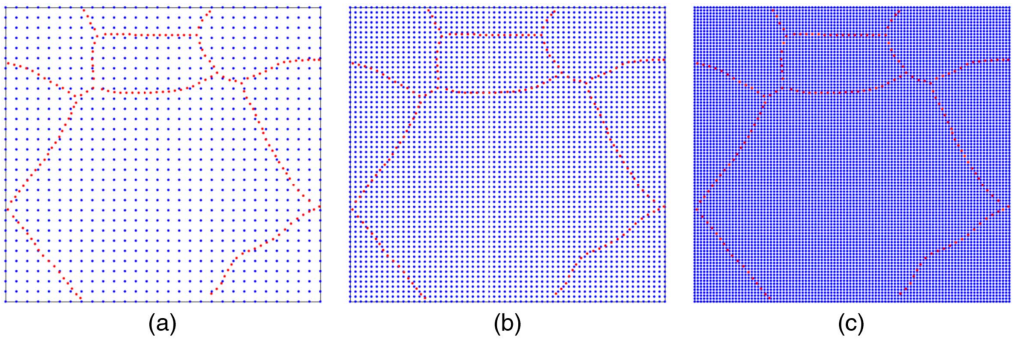

Fig. 13. Discretization for elastostatic stress analysis of polycrystalline structure with five grains using (a) 30×30 uniformly distributed background collocation points; (b) 60×60 uniformly distributed background collocation points; and (c) 100×100 uniformly distributed background collocation points.

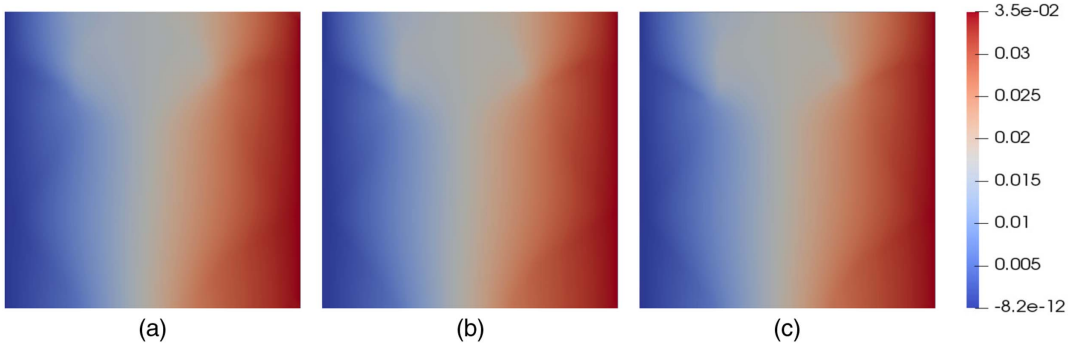

Fig. 14. Contour plots of x-direction displacement fields u_{xx} for the polycrystalline structure with 5 grains using (a) 30×30 collocation points; (b) 60×60 collocation points; and (c) 100×100 collocation points.

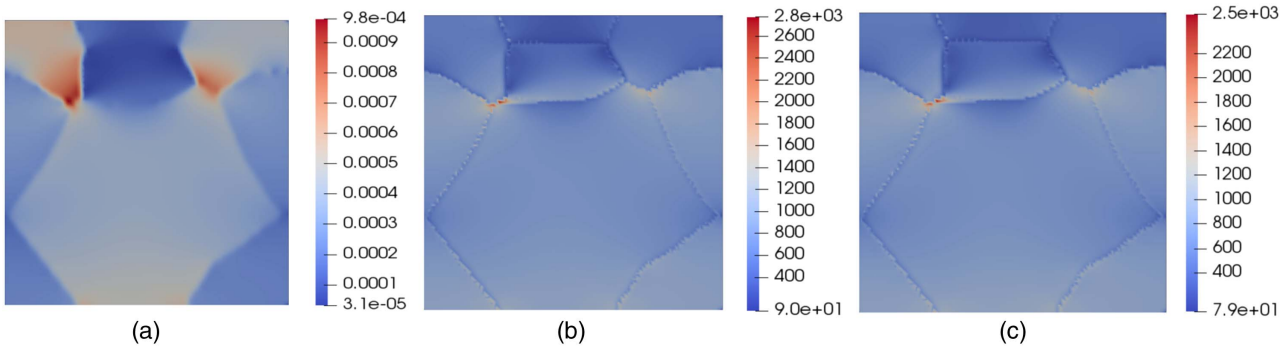

Fig. 15. Contour plots for polycrystalline structure with 5 grains by 100 × 100 collocation points: (a) strain ε_{xx}; (b) stress σ_{xx}; and (c) von Mises stress.

to determine confidently the appropriate termination time of the simulation.

Histograms of the area distribution during the evolution of 36 grains are shown in Fig. 7. In this data analysis, a log-normal distribution was used to fit these results, because this distribution is frequently used to describe the distribution of grain sizes in polycrystalline solids (Vaz and Fortes 1988). In order to obtain the area of each grain, each grain was approximated by a polygon, and the polygon areas were calculated; the shapes of grains in Fig. 6 show that this approximation was reasonable. Over the progression of time in Fig. 7, the shape of the histogram approaches a steady-state shape characterized by a high frequency of grains near the median size. This gives further evidence that the simulated solidification reached a steady state by $t = 8000\Delta t$ [Fig. 6(f)]. The average grain area reached a steady state by this time, as shown in Fig. 8, which plots the evolution of the average grain area as a function of time. The data in this figure were fitted to the equation $f(t) = (-8.841e + 05)t^{-1.303} + 5843$ by a multiparameter nonlinear least-squares fitting method. The results described here suggest the progression of the simulated solidification progress to a steady state, a conclusion that is further corroborated by the subsequently described evolution of the free energy.

The evolution of the total free energy over the simulated time up to 1,000 time steps, i.e., $1000\Delta t$, is shown in Fig. 9. Before time $t = 0$ and $t = 200\Delta t$, a rapid increase occurred in the free energy as the liquid phase was consumed by the growing solid grains. However, after $t = 200\Delta t$, a much slower increase in free energy occurred. After $t = 1000\Delta t$, the total free energy was sufficiently close to constant; i.e., the microstructure evolution was considered complete. The results from the free energy evolution and that of the total grain area are consistent and suggest the validity of the PDM-based phase field model analysis for polycrystalline growth.

As a final application for the polycrystalline solidification problem, we considered the effect of rigid inclusions on polycrystalline growth. For this analysis, the computational domain was discretized with 29,241 collocation points. The initial distribution of seed grains was chosen to be the same as the distribution in the previous example, which explains the similarity between the final arrangements of grains in the two microstructures. The inclusions were

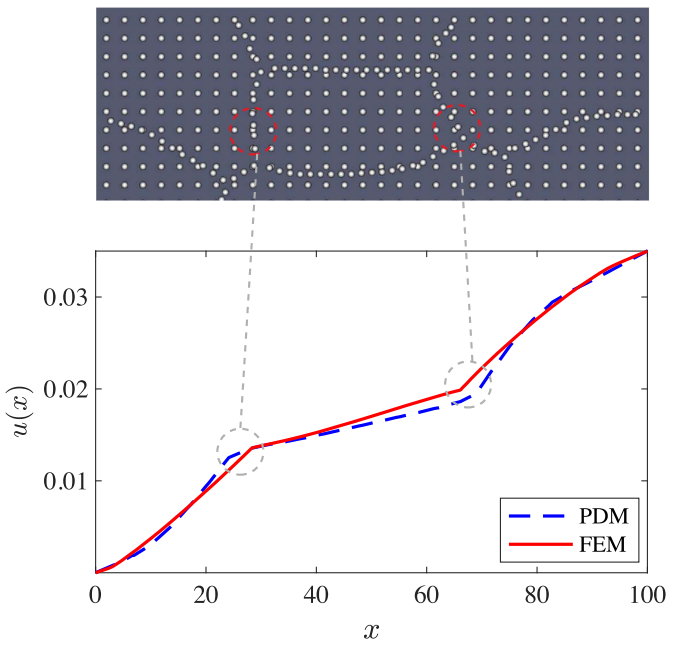

Fig. 16. PDM and the FEM displacement fields along Section 1 in Fig. 12.

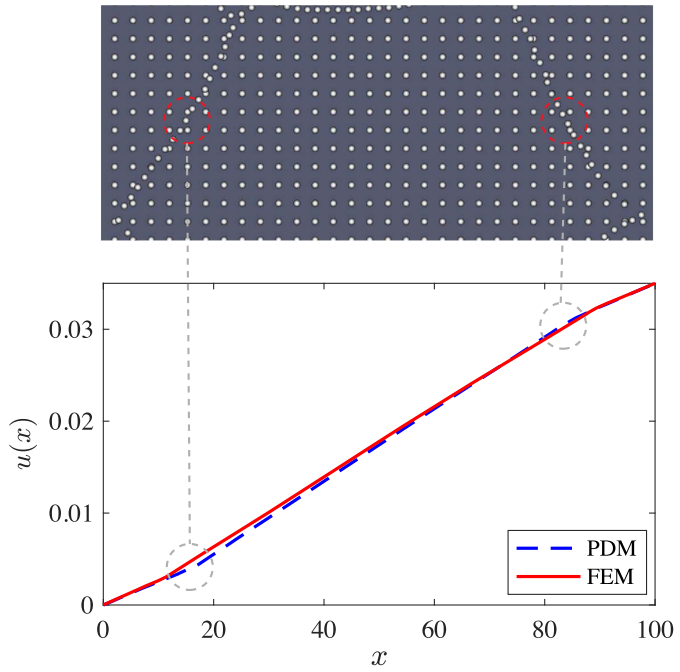

Fig. 17. PDM and the FEM displacement fields along Section 2 in Fig. 12.

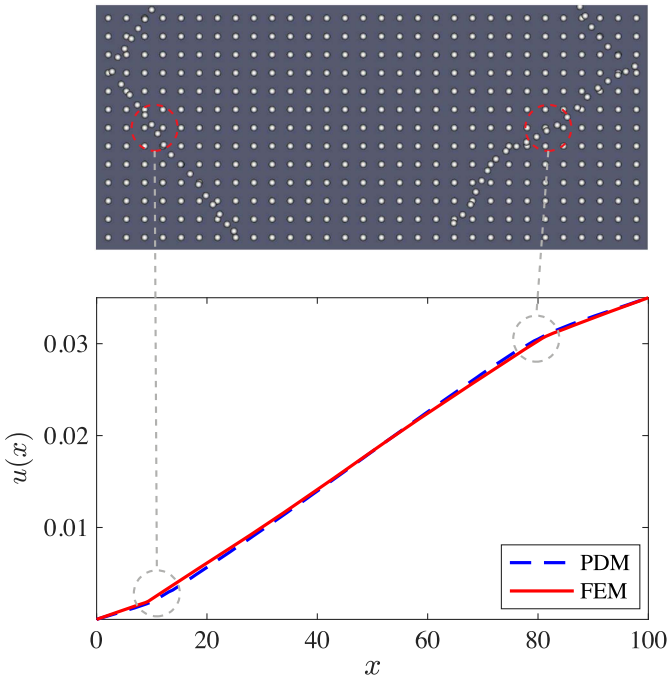

Fig. 18. PDM and the FEM displacement fields along Section 3 in Fig. 12.

modeled with the static phase field order parameters. In other words, the phase field variables φ_i corresponding to the inclusions were set to $\varphi_i = 1$ (i.e., fully solidified solids) during the phase field model analysis without updating them. Fig. 10 illustrates the evolution of the polycrystalline structure with six rigid inclusions at different time steps. Fig. 10(i) shows the final steady-state polycrystalline structure. As in the previous example with 36 grains, the evolution of the microstructure with inclusions exhibited dramatic grain growth during the first 200 time steps, corresponding to a sharp change in total free energy. Also similar to the previous example, after 200 time steps, the free energy began to approach a steady state and only more subtle changes occurred in the microstructure. In contrast to the previous examples, the inclusions near boundaries of inclusions at some locations had sharper, more angular, and less regular grain shapes.

The evolution of the total free energy up to 1,000 steps is shown in Fig. 11; again, after 1,000 steps the total free energy reached a plateau and the simulation stopped. The time history of the free energy evolution, which aligned with expectations, further suggests the validity of the PDM and the multiphase field model for simulating polycrystalline grain growth, even for this complicated model with rigid inclusions.

Polycrystalline Stress Analysis

In this section, we performed a stress analysis of the three polycrystalline structures obtained in the previous section, beginning with the polycrystalline structure predicted with five grains. The boundary conditions applied to the five grains structure are shown in Fig. 12; uniform displacement $\bar{u} = 3.5 \times 10^{-2}$ was prescribed at the right end of the computational domain. The Young's moduli of the grains were varied randomly so that the Young's modulus for each grain was different. The values chosen for the Young's moduli for the five grains had a Gaussian distribution with a mean value of 3.0×10^6 and standard deviation of 1.58×10^6.

For the study of discretization sensitivity, three different arrangements of collocation points were considered for the stress analysis of the five-grain polycrystalline structure with the PDM (Fig. 13). The discretization consisted of uniformly distributed collocation points over the entire domain (which served as the background collocation points) plus a set of concentrated collocation points superposed along grain boundaries. The resolution of the discretization was gradually increased, i.e., discretized with 30×30, 60×60, and finally 100×100 background collocation points, with the added collocation points along the grain boundaries [Figs. 13(a–c)]. Using these three different collocation point densities, the sensitivity of the PDM stress analysis to the level of discretization refinement was studied.

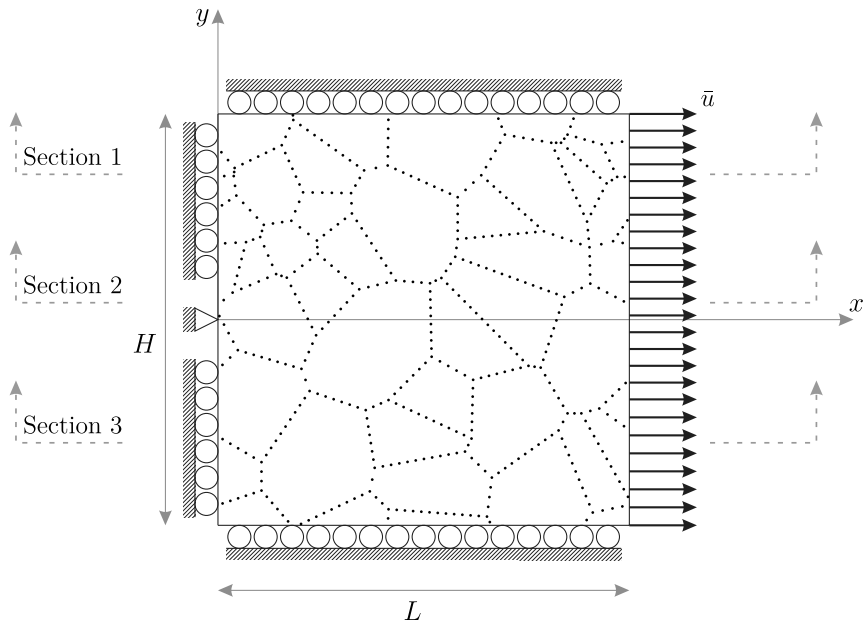

Fig. 19. Polycrystalline structure with 36 grains with boundary conditions, including the prescribed displacement at the right side.

The contour plots of the displacement in the x-direction for three different levels of refinement are shown in Fig. 14. The contour plots of strain (ε_{xx}), stress (σ_{xx}), and von Mises stress are shown in Fig. 15. All the results in these figures are qualitatively indistinguishable, indicating that the PDM had low sensitivity to the number of collocation points, i.e., discretization. These results verify the robustness of the proposed PDM for the polycrystalline stress analysis.

For further verification of the PDM, the computed displacement fields of the PDM were compared with the result of the finite-element method. More specifically, the computed displacement fields were compared between the PDM and the FEM at three different cross sections of the computational domain, subsequently referred to as Sections 1, 2, and 3. Fig. 16 shows the comparison of displacement results along a horizontal line passing through Grains 1 and 2 (i.e., φ_1 and φ_2), denoted Section 1. Similarly, Fig. 17

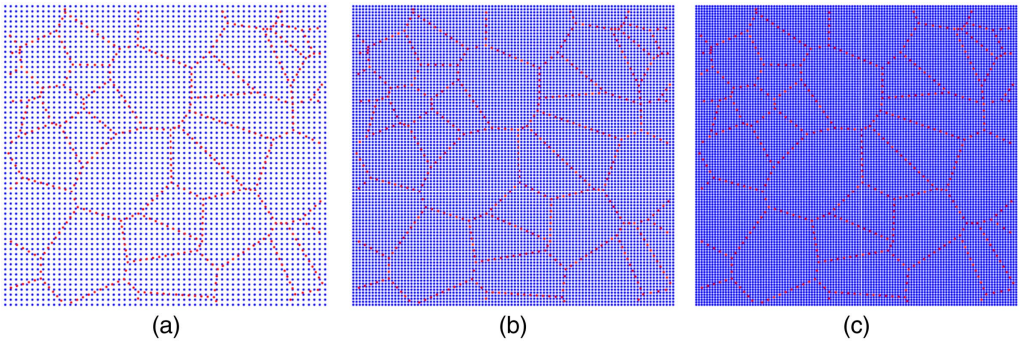

Fig. 20. Discretization for elastostatic stress analysis of polycrystalline structure with 36 grains using (a) 60 × 60 uniformly distributed background collocation points; (b) 100 × 100 uniformly distributed background collocation points; and (c) 120 × 120 uniformly distributed background collocation points.

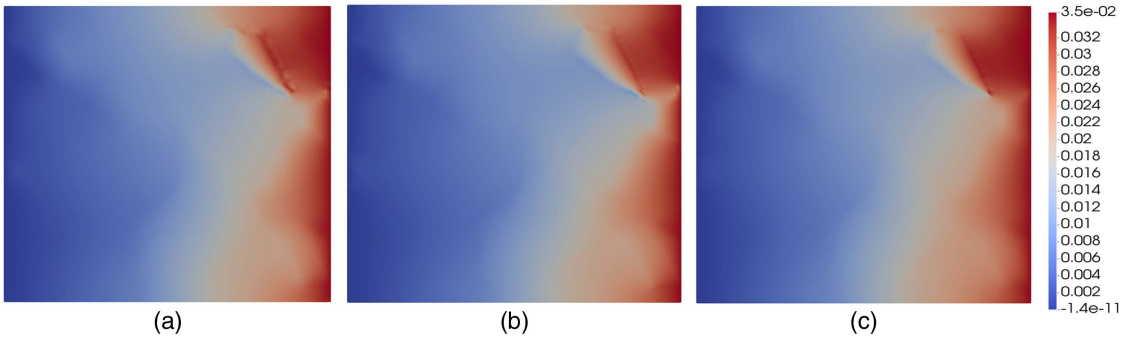

Fig. 21. Contour plots of the x-direction displacement fields u_{xx} for the polycrystalline structure with 36 grains using (a) 60 × 60 collocation points; (b) 100 × 100 collocation points; and (c) 120 × 120 collocation points.

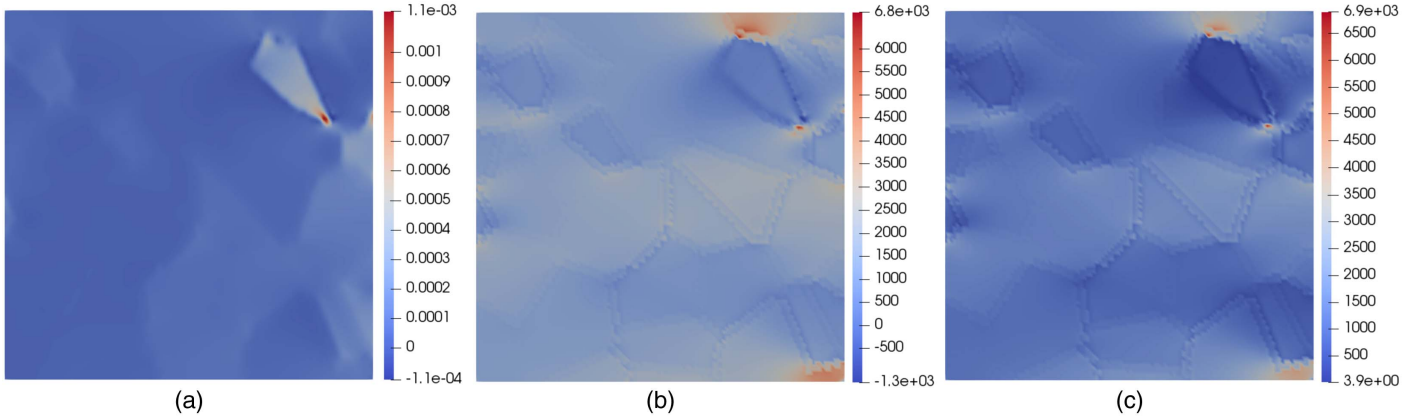

Fig. 22. Contour plots for polycrystalline structure with 36 grains by 120 × 120 collocation points: (a) strain ε_{xx}; (b) stress σ_{xx}; and (c) von Mises stress.

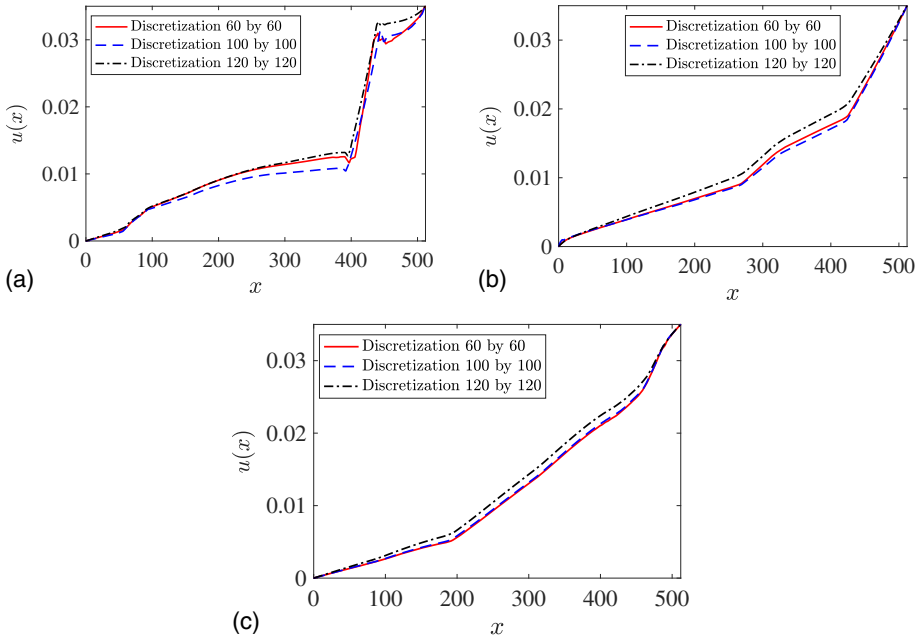

Fig. 23. PDM results at three different levels of discretization for displacement fields in Fig. 19 at (a) Section 1; (b) Section 2; and (c) Section 3.

compares the displacement fields for the PDM and the FEM along a horizontal line passing through Grains 3 and 5 (i.e., φ_3 and φ_5), denoted Section 2. Fig. 18 compares similar results for a line passing through Grains 4 and 5 (i.e., φ_4 and φ_5). The kinks in the plots originated from the discontinuity in material properties from one grain to another across grain boundaries. These kinks are the locations of the greatest discrepancy observed between the PDM and FEM results. However, this discrepancy was relatively small and was mainly due to the fact that the PDM has higher global continuity in the solution fields compared with C^0 continuity of the FEM. Despite these minor discrepancies, the PDM and FEM results agreed very well and were practically identical.

A similar approach was adopted for the stress analysis of the polycrystalline structure consisting of 36 grains. This structure was discretized with three different levels of refinement, i.e., 60×60, 100×100, and 120×120 uniformly distributed background collocation points. Again, extra collocation points were superposed along grain boundaries. The applied boundary conditions were similar to those in the previous example (Fig. 19), and the three different discretizations are shown in Fig. 20. The contour plots of the computed x-direction displacement fields and corresponding strain, stress, and von Mises stress fields are shown in Figs. 21 and 22, respectively. Regardless of the resolution of discretization and the complexity of the morphology of the grain boundaries, the PDM produced almost identical results and had very little discretization sensitivity (Fig. 23). Thus, the PDM effectively handled such a complex weak discontinuity emanating from the internal grain boundaries and produced a robust stress analysis. More results for the discretization sensitivity of the PDM within the similar context were given by Yoon et al. (2019), Song et al. (2018), and Yoon and Song (2014c).

As a final example, we considered the polycrystalline structure consisting of 30 grains with 6 inclusions; the boundary conditions applied to the computation are shown in Fig. 24. In this example, two different cases, i.e., Case 1 and Case 2, were considered to further investigate the effect of the relative rigidity of inclusions on the deformation of the polycrystalline materials. To this end, the same order of the Young's modulus for both grains and inclusions

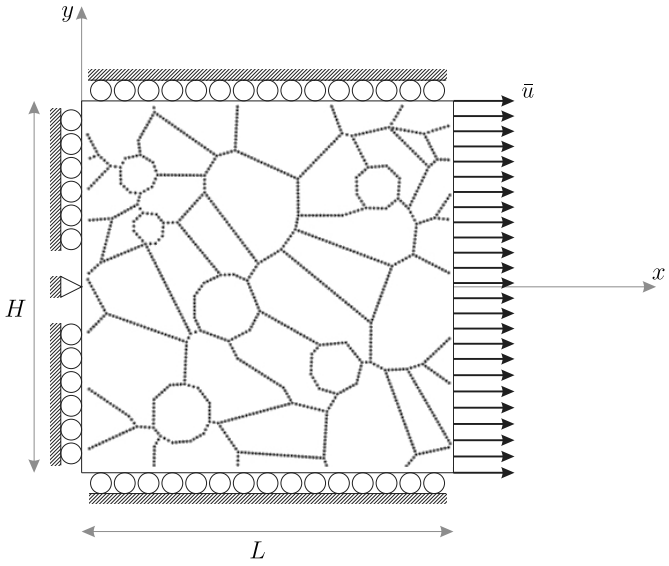

Fig. 24. Polycrystalline structure with 30 grains and 6 inclusions with boundary conditions, including the prescribed displacement at the right side.

were considered for Case 1. However, for Case 2, the Young's modulus of the inclusions was one order higher than that of the grains in order to study the aforementioned effect of the harder inclusions in a polycrystalline structure. Fig. 25 shows the arrangements of collocation points used for the PDM stress analysis of the polycrystalline structure with six inclusions.

The contour plots of displacement (u_{xx}) and von Mises stress considering the same order (i.e., Case 1) and one-order difference (i.e., Case 2) of material properties for grains and inclusions are shown in Figs. 26 and 27, respectively. The relatively harder inclusions significantly altered the deformation kinematics of the polycrystalline structure, including the stress concentration areas where failure of the polycrystalline material is likely to initiate. Overall,

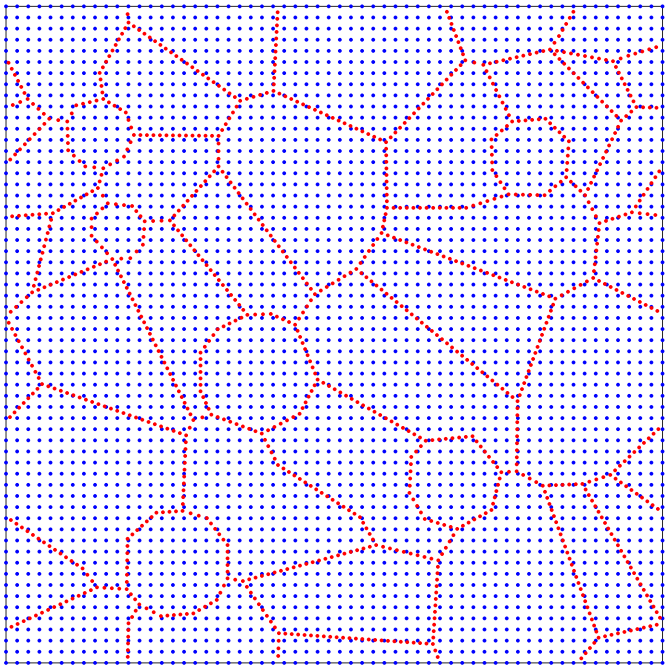

Fig. 25. Discretization for elastostatic analysis of polycrystalline structure with 30 grains and 6 inclusions using 60×60 uniformly distributed background collocation points.

the PDM is sufficiently robust to provide the type of detailed stress analysis necessary for investigating these phenomena. However, further investigations of the relationship between failure behaviors of the polycrystalline materials and the microscale inclusions remain part of the authors' future work.

Conclusion

In this paper, the PDM was used to study grain growth in a polycrystalline solid and stress analysis of the formed solid. The PDM results related to the polycrystalline grain growth problems were shown to be accurate based on the evolution of average grain area and total free energy. The PDM results from the stress analysis were compared with and verified by FEM results, which showed the high accuracy of the PDM in computing both displacements and stresses in the problems presented. The results of this study also demonstrate that the PDM has low discretization sensitivity.

As a meshfree point collocation method, the PDM does not require any kind of mesh, which obviates numerical integration. In contrast to other meshfree methods, the PDM does not require direct calculation of derivatives of shape functions, i.e., approximate derivatives from the moving least-squares approximation provide all order of derivatives needed. As a consequence, numerical cost is reduced considerably compared with direct calculation of derivatives. As evidenced by its unique advantages as a numerical method, as well as the results from this paper, the PDM shows

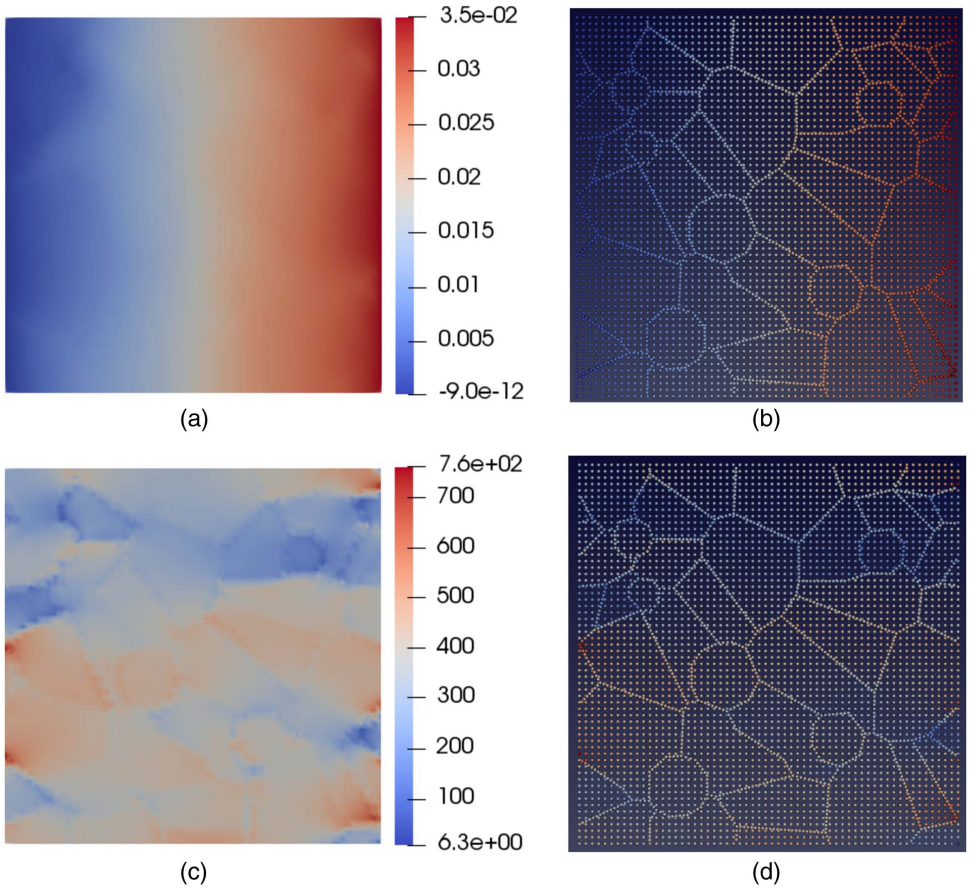

Fig. 26. Contour plot for the 30 grains and 6 inclusions which have the same order of Young's moduli: (a and b) x-direction displacement fields u_{xx}; and (c and d) are von Mises stress.

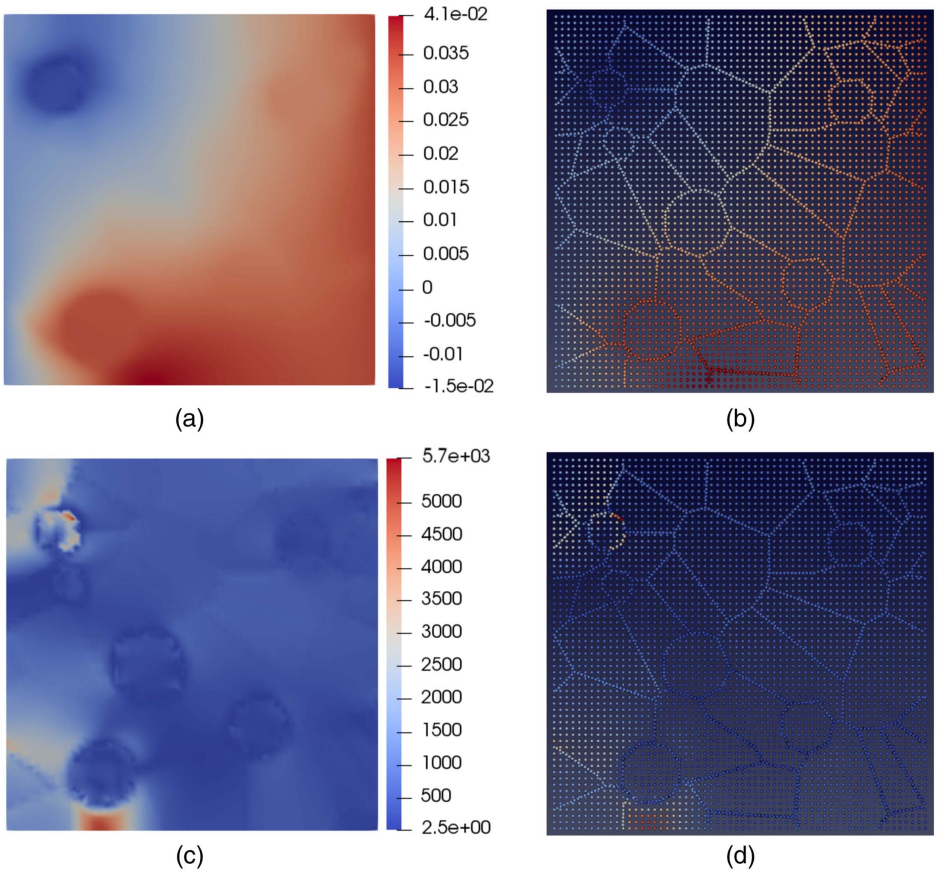

Fig. 27. Contour plot for the 30 grains and 6 inclusions which have different orders of Young's moduli: (a and b) are x-direction displacement fields u_{xx}; and (c and d) are von Mises stress.

promise to solve complex problems in solid mechanics that require local refinement and dynamic adaptivity. To use these advantages of the PDM, our future work will focus on applying the PDM to various problems involving moving interfaces and intricate geometry, as well as higher-order derivatives.

Acknowledgments

The fourth and fifth authors acknowledge support for this work by the Office of Naval Research (ONR) through the Naval Research Laboratory's core funding. The fifth author also acknowledges support for this work through the Idaho National Laboratory (INL) Laboratory Directed Research and Development Program (LDRD) under the Department of Energy (DOE) Idaho Operation Office Contract DE-AC07-05ID14517.

References

Allen, S. M., and J. W. Cahn. 1979. "A microscopic theory for antiphase boundary motion and its application to antiphase domain coarsening." *Acta Metall.* 27 (6): 1085–1095. https://doi.org/10.1016/0001-6160(79)90196-210.1016/0001-6160(79)90196-2.

Aluru, N. 2000. "A point collocation method based on reproducing kernel approximations." *Int. J. Numer. Methods Eng.* 47 (6): 1083–1121. https://doi.org/10.1002/(SICI)1097-0207(20000228)47:6<1083::AID-NME816>3.0.CO;2-N.

Atluri, S. N., H.-G. Kim, and J. Y. Cho. 1999. "A critical assessment of the truly Meshless local Petrov-Galerkin (MLPG), and Local Boundary Integral Equation (LBIE) methods." *Comput. Mech.* 24 (5): 348–372. https://doi.org/10.1007/s004660050457.

Belytschko, T., Y. Y. Lu, and L. Gu. 1994. "Element-free Galerkin methods." *Int. J. Numer. Methods Eng.* 37 (2): 229–256. https://doi.org/10.1002/nme.1620370205.

Chen, J., V. Kotta, H. Lu, D. Wang, D. Moldovan, and D. Wolf. 2004. "A variational formulation and a double-grid method for meso-scale modeling of stressed grain growth in polycrystalline materials." *Comput. Methods Appl. Mech. Eng.* 193 (12–14): 1277–1303. https://doi.org/10.1016/j.cma.2003.12.020.

Duarte, C. A., and J. T. Oden. 1996. "H-p clouds—An h-p meshless method." *Numer. Methods Partial Differ. Equations* 12 (6): 673–705. https://doi.org/10.1002/(SICI)1098-2426(199611)12:6<673::AID-NUM3>3.0.CO;2-P.

Fan, D., and L.-Q. Chen. 1997. "Computer simulation of grain growth using a continuum field model." *Acta Mater.* 45 (2): 611–622. https://doi.org/10.1016/S1359-6454(96)00200-510.1016/S1359-6454(96)00200-5.

Fu, Y., J. G. Michopoulos, and J.-H. Song. 2017. "Bridging the multi phase-field and molecular dynamics models for the solidification of nano-crystals." *J. Comput. Sci.* 20 (May): 187–197. https://doi.org/10.1016/j.jocs.2016.10.014.

Gingold, R. A., and J. J. Monaghan. 1977. "Smoothed particle hydrodynamics: Theory and application to non-spherical stars." *Mon. Not. R. Astron. Soc.* 181 (3): 375–389. https://doi.org/10.1093/mnras/181.3.375.

Hillman, M., and J.-S. Chen. 2016. "An accelerated, convergent, and stable nodal integration in Galerkin meshfree methods for linear and nonlinear mechanics." *Int. J. Numer. Methods Eng.* 107 (7): 603–630. https://doi.org/10.1002/nme.5183.

Kim, D. W., and Y. Kim. 2003. "Point collocation methods using the fast moving least-square reproducing kernel approximation." *Int. J. Numer. Methods Eng.* 56 (10): 1445–1464. https://doi.org/10.1002/nme.618.

Kim, H.-K. 2004. "Point collocation method based on the FMLSRK approximation for electromagnetic field analysis." *IEEE Trans. Magn.* 40 (2): 1029–1032. https://doi.org/10.1109/TMAG.2004.824612.

Lee, S.-H., K.-H. Kim, and Y.-C. Yoon. 2016. "Particle difference method for dynamic crack propagation." *Int. J. Impact Eng.* 87 (Jan): 132–145. https://doi.org/10.1016/j.ijimpeng.2015.06.001.

Lee, S.-H., and Y.-C. Yoon. 2004. "Meshfree point collocation method for elasticity and crack problems." *Int. J. Numer. Methods Eng.* 61 (1): 22–48. https://doi.org/10.1002/nme.1053.

Li, S., and W. K. Liu. 1999a. "Reproducing kernel hierarchical partition of unity, Part I—Formulation and theory." *Int. J. Numer. Methods Eng.* 45 (3): 251–288. https://doi.org/10.1002/(SICI)1097-0207(19990530)45:3<251::AID-NME583>3.0.CO;2-I.

Li, S., and W. K. Liu. 1999b. "Reproducing kernel hierarchical partition of unity, Part II—Applications." *Int. J. Numer. Methods Eng.* 45 (3): 289–317. https://doi.org/10.1002/(SICI)1097-0207(19990530)45:3<289::AID-NME584>3.0.CO;2-P.

Liu, W. K., S. Jun, and Y. F. Zhang. 1995. "Reproducing kernel particle methods." *Int. J. Numer. Methods Fluids* 20 (8–9): 1081–1106. https://doi.org/10.1002/fld.1650200824.

Liu, W. K., Y.-C. Yoon, T. Belytschko, and S.-H. Lee. 2007. "Meshfree point collocation method with intrinsic enrichment for interface problems." *Comput. Mech.* 40 (6): 1037–1052. https://doi.org/10.1007/s00466-007-0162-1.

Nayroles, B., G. Touzot, and P. Villon. 1992. "Generalizing the finite element method: Diffuse approximation and diffuse elements." *Comput. Mech.* 10 (5): 307–318. https://doi.org/10.1007/BF00364252.

Onate, E., S. Idelsohn, O. Zienkiewicz, and R. Taylor. 1996. "A finite point method in computational mechanics. applications to convective transport and fluid flow." *Int. J. Numer. Methods Eng.* 39 (22): 3839–3866. https://doi.org/10.1002/(SICI)1097-0207(19961130)39:22<3839::AID-NME27>3.0.CO;2-R.

Simmons, J., C. Shen, and Y. Wang. 2000. "Phase field modeling of simultaneous nucleation and growth by explicitly incorporating nucleation events." *Scr. Mater.* 43 (10): 935–942. https://doi.org/10.1016/S1359-6462(00)00517-0.

Song, J.-H., Y. Fu, T.-Y. Kim, Y.-C. Yoon, J. G. Michopoulos, and T. Rabczuk. 2018. "Phase field simulations of coupled microstructure solidification problems via the strong form particle difference method." *Int. J. Mech. Mater. Des.* 14 (4): 491–509. https://doi.org/10.1007/s10999-017-9386-1.

Vaz, M. F., and M. Fortes. 1988. "Grain size distribution: The lognormal and the gamma distribution functions." *Scr. Metall.* 22 (1): 35–40. https://doi.org/10.1016/S0036-9748(88)80302-8.

Wang, D., J. Wang, and J. Wu. 2018. "Superconvergent gradient smoothing meshfree collocation method." *Comput. Methods Appl. Mech. Eng.* 340 (Oct): 728–766. https://doi.org/10.1016/j.cma.2018.06.021.

Yoon, Y.-C., S.-H. Lee, and T. Belytschko. 2006. "Enriched meshfree collocation method with diffuse derivatives for elastic fracture." *Comput. Math. Appl.* 51 (8): 1349–1366. https://doi.org/10.1016/j.camwa.2006.04.010.

Yoon, Y.-C., W. K. Liu, and T. Belytschko. 2007. "Extrinsic meshfree approximation using asymptotic expansion for interfacial discontinuity of derivative." *J. Comput. Phys.* 221 (1): 370–394. https://doi.org/10.1016/j.jcp.2006.06.023.

Yoon, Y.-C., P. Schaefferkoetter, T. Rabczuk, and J.-H. Song. 2019. "New strong formulation for material nonlinear problems based on the particle difference method." *Eng. Anal. Boundary Elem.* 98 (Jan): 310–327. https://doi.org/10.1016/j.enganabound.2018.10.015.

Yoon, Y.-C., and J.-H. Song. 2014a. "Extended particle difference method for moving boundary problems." *Comput. Mech.* 54 (3): 723–743. https://doi.org/10.1007/s00466-014-1029-x.

Yoon, Y.-C., and J.-H. Song. 2014b. "Extended particle difference method for weak and strong discontinuity problems: Part I. Derivation of the extended particle derivative approximation for the representation of weak and strong discontinuities." *Comput. Mech.* 53 (6): 1087–1103. https://doi.org/10.1007/s00466-013-0950-8.

Yoon, Y.-C., and J.-H. Song. 2014c. "Extended particle difference method for weak and strong discontinuity problems: Part II. Formulations and applications for various interfacial singularity problems." *Comput. Mech.* 53 (6): 1105–1128. https://doi.org/10.1007/s00466-013-0951-7.

Zhu, T., J. Zhang, and S. Atluri. 1998. "A meshless local boundary integral equation (LBIE) method for solving nonlinear problems." *Comput. Mech.* 22 (2): 174–186. https://doi.org/10.1007/s004660050351.